ROYAL SOCIETY OPEN SCIENCE

royalsocietypublishing.org/journal/rsos



Research

**Cite this article:** Hazmi B, Rashid U, Sabater MJ, Simbaña Alvaro GM, Hinchiranan N, Chotirattanachote A, Ngamcharussrivichai C. 2026 Carbonized UiO-66 with Ni nanoparticles for PFAD deoxygenation to green diesel hydrocarbons: characterization, optimization and deactivation analysis. *R. Soc. Open Sci.* **13**: 250756.
https://doi.org/10.1098/rsos.250756

Received: 16 April 2025
Accepted: 3 November 2025

**Subject Category:**
Chemistry

**Subject Areas:**
materials science, green chemistry, nanotechnology

**Keywords:**
metal–organic framework, synthesis, deoxygenation, response surface methodology, hydrocarbons, green biofuel

**Author for correspondence:**
Umer Rashid
e-mails: umerrashid@ucsiuniversity.edu.my; dr.umer.rashid@gmail.com

Supplementary material is available online at https://doi.org/10.6084/m9.figshare.c.8156466.

THE ROYAL SOCIETY PUBLISHING

# Carbonized UiO-66 with Ni nanoparticles for PFAD deoxygenation to green diesel hydrocarbons: characterization, optimization and deactivation analysis

Balkis Hazmi[1], Umer Rashid[2,3,4], Maria J. Sabater[5], Grace Marianela Simbaña Alvaro[5], Napida Hinchiranan[3], Atikhun Chotirattanachote[3] and Chawalit Ngamcharussrivichai[3,4]

[1]Institute of Nanoscience and Nanotechnology, Universiti Putra Malaysia, Serdang, Selangor, Malaysia
[2]Faculty of Applied Sciences, UCSI University, Cheras, Federal Territory of Kuala Lumpur, Malaysia
[3]Department of Chemical Technology, and [4]Centre of Excellence in Catalysis for Bioenergy and Renewable Chemicals (CBRC), Faculty of Science, Chulalongkorn University, Bangkok, Thailand
[5]Instituto de Tecnología Química, Valencia, Spain

UR, 0000-0001-6224-413X; GMSA, 0009-0007-3861-2298

Fabricating effective reusable catalysts for biomass deoxygenation is essential for sustainable fuel production. In this study, Ni nanoparticles (15–25 wt%) were incorporated into UiO-66 through solvothermal synthesis, followed by partial carbonization at 300°C to improve thermal stability, dispersion and catalytic efficiency in palm fatty acid distillate deoxygenation. Structural analysis confirmed that the UiO-66 framework remained intact after Ni incorporation, with X-ray photoelectron spectroscopy indicating well-dispersed Ni species ($Ni2p_{3/2}$ at 855.6–856.7 eV). The acid–base characteristics and high surface area supported the cleavage of C–O and C–C bonds. Among the catalysts tested, C-UiO-66@Ni-20wt% showed the best performance, achieving an 87.65% hydrocarbon yield under conditions (3.14 h, 3.28 wt% catalyst, 340°C) optimized by response surface methodology.

The reliability of the model was confirmed by a high $R^2$ value (99.47%) and statistical significance ($p < 0.0001$). The catalyst maintained stable activity over seven cycles, with only a 2–7% yield reduction per cycle, before significant deactivation occurred in the eighth cycle owing to pore blockage and active site agglomeration. This study illustrates that Ni-doped UiO-66, with its balanced acidity, structural integrity and efficiency at low temperatures, is a promising catalyst for scalable biofuel production, offering both high reactivity and reusability.

# 1. Introduction

The fossil fuel reserves around the world are depleting due to high consumption of ≥88% over years for industrialization, automobile and electricity generation. Conventional fuel exploration is still actively underway to meet the demands supply, yet experts believe that the reserves projected to sustain for no longer than five decades [1]. Moreover, exploitation of energy derived from non-renewable sources results in the emission of greenhouse gases (GHGs) which pose environmental harm, particularly in terms of contributing to climate change [2,3]. Since then, eco-friendly alternative energy sources have gained attention to address the anticipated fossil fuel shortage in the future while reducing GHG emissions. Therefore, extensive research and development has been executed for producing diverse alternative energy derived from green resources, for instance biomass-based biofuel, owing to its sustainability and emitting neutral $CO_2$ resources [4].

Interestingly, biomass from inedible oil, animal fats, waste cooking oil, etc., are composed of fatty acids that can be converted into liquid renewable biofuels [5,6]. These biofuels can be utilized in current biodiesel engines without significant modifications. Unfortunately, esterified biodiesel fatty methyl esters contain 30–40% of oxygenated groups that easily oxidize over time and leads to poor cold-flow properties which are less favourable for a fuel injection compression engine [7]. Therefore, upgrading the fatty acids into alkane hydrocarbons of C13–C18, also known as green-diesel, via deoxygenation significantly improves the physiochemical properties that are similar to those of fossil diesel [8]. There are two routes for free hydrogen deoxygenation reaction, namely decarboxylation (DCX) and decarbonylation (DCN). Both pathways involve removing the fatty acid oxygenated group and conversion into alkanes and alkenes, respectively, by losing one carbon atom from the parent structure [9], as shown in the following:

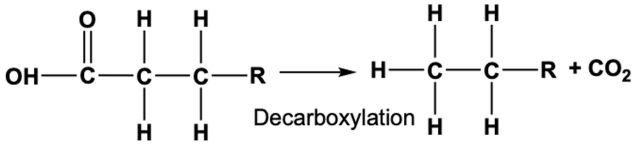


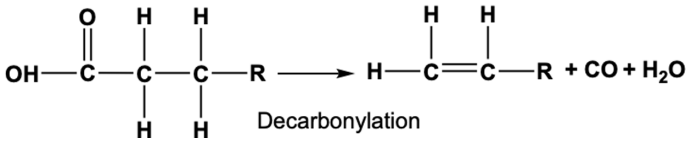


The deoxygenation of fatty acids into hydrocarbons operates at high temperature to break the oxygenated bonds and literally requires catalysis to accelerate the reaction process and to achieve selectivity of desired products at maximum yield. The conventional catalysts for the hydrocarbon deoxygenation process are primarily functionalized with noble metals (Pt, Pd, Rh, Ru, Ti) or sulfided metals ($MoS_2$, NiMoS, CoMoS) supported on metal oxides or activated carbon [10–13]. These catalysts possess acidic properties that are highly reactive at low reaction temperature (<300°C) and selective for the formation of deoxygenated compounds, inducing C–O and C–C bond cleavages subsequently forming $CO_2$ and $H_2O$ as byproducts [14,15]. Mesoporous catalytic precursors such as ZSM-5, MCM-48 and H-Beta were deposited with Ni/Pt to investigate the catalytic effectiveness of hydrocarbon conversion from Jatropha oil. These catalysts exhibited large surface area of >300 $m^2\ g^{-1}$ and the total acidity adsorption measured using TPD-$NH_3$ was recorded giving the following sequence: Ni/Pt/ZSM-5 (1.56 mmol $g^{-1}$) > Ni/Pt/MCM-48 (1.48 mmol $g^{-1}$) > Ni/Pt/H-beta zeolites (1.40 mmol $g^{-1}$), which influenced the selectivity yield (%) of C15–C18 at 96.7%, 90.5% and 88%, respectively [16]. Nevertheless, the noble metal supported catalysts utilization for industrial-scale production is not feasible due

to high operating cost attributed by expensive catalyst materials, whereas the sulfide-based catalysts are not eco-friendly owing to sulfur leaching which leads to unwanted sulfur-containing products. A study by Brillouet *et al.* discovered the formation of 1-decanethiol intermediate which occurred during the HDO catalytic reaction between decanoic acid and $Mo/Al_2O_3$ sulfide catalyst due to catalyst chemical instability (leaching) before adding Ni and Co promoters to strengthen the catalyst structure [17]. That is why scientists are shifting from conventional catalyst utilization to cost-viable catalysts derived from transition metals (Ni, Mo, Co, Fe, etc.) with a slight modification for the deoxygenation reaction [18].

Transition metals have Lewis–Brønsted acid properties that can promote deoxygenation; simultaneous decarboxylation and decarbonylation pathways to deoxygenate fatty acids into hydrocarbons. For instance, alkane diesel-like derived from Neem oil was hydrodeoxygenated in the presence of $Ni/MgSiO_3$ catalyst under optimized reaction conditions (15 wt% catalyst loading, 300°C, 8 bar of $H_2$ and 3 h) giving up to 72.34% total alkane with a notable selectivity towards C15 and C17 and this reaction was repeated six times (38.20%) [19]. Shi *et al.* also studied the effectiveness of Ni as an active site that impregnated on $MgO–Al_2O_3$ support for deoxygenation of oleic acid. The catalytic deoxygenation screening showed that $Ni(10\%)/MgO–Al_2O_3$ catalyst had mild Brønsted-rich acidic sites (27.36 mmol $g^{-1}$), which effectively afforded the highest hydrocarbon conversion (92.12%) and olefin (57.37%) and green biodiesel content (75.9%) [20]. De Rossa *et al.* synthesized sustainable catalysts, Co/EAC catalyst derived from impregnating Co over Macauba endocarp activated carbon for catalytic deoxygenating of Macauba oil. In this way, the Macauba oil was selectively converted into bio-hydrocarbons (96.7%, C10–C22), kerosene (47.3%, C8–C16) and gasoline (13.1%, C4–C12) within 2 h, at 350°C by $H_2$ pressure of 30 bar [21]. The side effect of utilizing acidic catalysts in this reaction is carbon deposition, which can lead to coke formation on the catalyst's surface as it can chemically deactivate the catalyst, leading to a reduction in hydrocarbon selectivity over multiple uses and, consequently, reducing the catalytic performances [22]. A study of red mud supported nickel catalyst (Ni/RM) for HDO of palmitic acid gave 100% alkane conversion and selectivity towards deoxygenated alkanes in both cases under optimized conditions (0.04 g catalyst loading, 300°C, 4 MPa of $H_2$, 4 h) and but after four and five reuses, it was observed that the conversion and selectivity of alkanes declined, by obtaining more hexadecanol (a fatty alcohol intermediate), showing the loss of catalytic effectiveness and being almost deactivated [8]. Fatty alcohols are also useful as indispensable intermediates especially in the production of pharmaceuticals, detergents, cosmetics and lubricants [23]. A study by Quintero-Ramos *et al.* successfully converted ethyl stearate into 1-octadecanol via catalytic hydrogenation using a stable and active catalyst of Ru incorporated W/Zr (Ru (1.3)/W(33)/Zr) at 175°C and 40 bar of $H_2$ by achieving highest turnover frequency of approximately 3.4 [23]. The catalyst deactivation analysis of 40 wt%Fe/HMS after use revealed carbon deposition on the catalyst surface by means of thermogravimetric analysis, showing two main weight losses at 50–400°C and 450–600°C which were attributed to soft and hard coke respectively, whereas elemental analysis via energy-dispersive X-ray analysis (EDX) showed a notable Fe reduction from 36.9 to 10.4 wt% due to active site leaching upon multiple deoxygenation reactions [24].

The current catalysis science has been improved with the nanotechnology discovery due to diverse novel nanomaterial frameworks with excellent active sites that contribute for high catalytic selectivity and catalyst reusability. In this regard, metal–organic frameworks (MOFs) have great potential as heterogeneous catalysts for a range of organic transformations. MOFs are materials characterized by their porous nature, consisting of metal ions or clusters of metal oxides serving as nodes, whereas organic ligands function as linkers [25]. Scientists have focused on MOFs owing to their unique structural and functional properties [26]. In catalytic applications, MOFs feature an extensive surface area and pore size that improve the diffusion and interfacial contact between the active sites and reactants [27]. Moreover, the adaptability of MOF design enables the alteration of their catalytic sites and surface charges to suit specific reactions, facilitating the adsorption and desorption of fatty acids for the production of green fuel [28]. Shi *et al.* synthesized ultrathin Ni-Sn IMC@C-700, a catalyst derived from MOF-74 carbon, which contained an encapsulated Ni-Sn alloy, and it was applied as a catalyst during the FAME deoxygenation reaction by giving 93.1% of diesel-like hydrocarbon (*n*-C15 and *n*-C16) yield at 330°C. The catalyst was reused without significant catalytic deactivation within five reaction cycles [29]. A novel bimetallic MOF catalyst, NiZn-MC@CB supported on carbon black waste, successfully catalysed the deoxygenation reaction of stearic acid by achieving 100% of conversion and the following selectivity fraction: 51.4% alkanes, 29.3% olefins and 19.3% aromatics. Zhang *et al.* [30] reported that NiZn-MC@CB catalyst exhibited Lewis (1437 $cm^{-1}$, 1445 $cm^{-1}$) and Brønsted acid sites (1537 $cm^{-1}$) that mainly facilitated deoxygenation and cracking reactions during the conversion

of stearic acids into hydrocarbons. A comparative study of oleic acid hydrotreatment showed that MOF-based Co-NP/NC reached 99.6% conversion and 99.6% alkane yield, higher than those obtained with conventional Co/AC catalyst (76.8% conversion and 14.9% total alkane yield) [31].

MOF-based catalysts are recognized as promising materials in catalysis owing to their large surface area, which supports active sites and facilitates reaction interactions. However, thermal stability remains a challenge for MOFs, as their frameworks, formed by coordination bonds between organic linkers and metal ions, tend to collapse under the high temperatures often required for catalytic deoxygenation reaction. Partial carbonization offers a solution by enhancing the thermal stability of MOFs without significantly altering their original structure. Furthermore, this process transforms the MOF into a carbonized porous framework with controlled pore sizes, enabling improved dispersion of heteroatom dopants during impregnation. Considering these factors, we devised an easy method to create innovative and durable C-UiO-66@Ni catalysts featuring well-distributed nanoparticles. To accomplish this, we selected Ni-MOFs with precisely arranged metal ions confined within cages as starting materials, ensuring ample active sites and preventing clumping of Ni nanoparticles during the pyrolysis process. Hence, a series of MOF-nanostructured UiO-66 derived catalysts with nickel nanoparticles (Ni = 15, 20 and 25 wt%) were activated by partial carbonization at 300°C to improve the chemical stability and reactivity. The series of as-prepared C-UiO-66@Ni nanocatalysts were utilized in the catalytic deoxygenation of highly acidic feedstock such as palm fatty acid distillate (PFAD) in solventless and inert conditions for hydrocarbons production. The series of C-UiO-66@Ni catalysts were completely characterized using different conventional techniques to find a relationship between physicochemical properties towards catalytic activity and hydrocarbons selectivity. The catalytic performance screening tests were carried out to select an optimum catalyst for further deoxygenation optimization study. Hence, the catalytic deoxygenation optimization using C-UiO-66@Ni-20wt% was performed using response surface methodology–central composite design (RSM-CCD) to study the interaction between reaction time, catalyst loading and temperature in response of hydrocarbon yield and selectivity. The optimized deoxygenation parameters were determined using response optimizer after completing 20 experiment runs, and the validation tests were conducted in triplicate to ensure reproducibility and reliability. Then, recovery and reusability studies of C-UiO-66@Ni-20wt% were carried out, followed by spent catalyst deactivation characterization.

# 2. Material and methods

## 2.1. Reagent and materials

All solvents and chemicals, methanol (99.8%, R&M), *n*-hexane (99.8%, R&M), dimethylformamide (99.5%, R&M), zirconium oxychloride octahydrate ($ZrOCl_2.8H_2O$, AR grade, QRëC), benzene-1,4-dicarboxylic acid (BDC, 98.0%, Sigma-Aldrich), nickel nitrate ($Ni(NO_3)_2.6H_2O$, 98.0%, R&M), acetic acid ($CH_3COOH$, 98%, R&M) and hydrochloric acid (HCl, 37%, R&M), were of analytical reagent grade and used without further purification. The PFAD was acquired from a palm oil mill in Mempaga, Malaysia. Prior to the deoxygenation rection process, the PFAD physicochemical characteristics were studied and summarized as tabulated in table 1.

## 2.2. Catalyst preparation

### 2.2.1. Preparation of UiO-66

7.5 mmol of terephthalic acid was mixed with 30 ml of DMF and stirred at 550 r.p.m. for 15 min at room temperature. Then the metal coordination cluster salt, $ZrOCl_2.8H_2O$ (5 mmol), dissolved in ethanol was mixed with the previous terephthalic acid solution followed by the addition of modulators (2 ml of acetic acid and 1.5 ml of hydrochloric acid) to enhance the reproducibility and crystallinity of UiO-66. The resulting solution mixture was sonicated for 3 h, and then transferred into a Teflon-lined autoclave and heated at 160°C for 12 h. The resulting white suspension was centrifuged, and the solvent was removed by decantation to afford compound UiO-66. The latter was washed three times with warm ethanol to remove excess DMF and unreacted terephthalic acid. Then, pure UiO-66 MOF was activated in a vacuum oven at 120°C for 24 h and stored in a desiccator.

**Table 1.** Physicochemical properties of PFAD feedstock.

| physicochemical analysis | |
|---|---|
| **properties** | **value** |
| free fatty acid (FFA, %) | 86.54 |
| acid value (mg KOH $g^{-1}$) | 173.08 |
| saponification value | 213.15 |
| molecular weight (g $mol^{-1}$) | 263.19 |
| density (g $cm^{-3}$) | 0.86 |
| moisture content (%) | 0.65 |
| viscosity at 40°C (cSt) | 28 |
| **fatty acids profile** | |
| **fatty acid** | **composition (%)** |
| myristic acid, C14:0 | 0.82 |
| palmitic acid, C16:0 | 49.13 |
| stearic acid, C18:0 | 4.01 |
| oleic acid, C18:1 | 40.72 |
| linoleic acid, C18:2 | 5.32 |
| saturated fatty acid | 53.96 |
| unsaturated fatty acid | 46.04 |

### 2.2.2. Preparation of C-UiO-66@Ni catalyst

The powdered UiO-66 was utilized as catalyst precursor for synthesizing UiO-65@NiO catalysts via wet impregnation method. An ethanolic UiO-66 suspension was prepared by ultrasonicating 5 g of UiO-66 and 30 ml of ethanol. The UiO-66 suspension was agitated at 500 r.p.m. and dropwise of $Ni(NO_3)_2.6H_2O$ solution (pre-weighed salt as 15, 20 and 25 wt%) was deposited based on weight of UiO-66. The mixture was continuously agitated 6 h followed by oven drying at 75°C for 12 h. The dried composite was partially carbonized at 300°C (3°C $min^{-1}$) for 3 h under nitrogen flow (2°C $min^{-1}$). The synthesized catalysts were named as C-UiO-66@Ni-15wt%, C-UiO-66@Ni-20wt% and C-UiO-66@Ni-25wt%. The reactivity and selectivity of synthesized catalysts were carried out for testing via catalytic deoxygenation reaction.

## 2.3. Catalyst characterization

Functional group determination was carried out using the Fourier-transform infrared spectroscopy technique with a PerkinElmer Spectrum 100 analyser coupled with attenuated total reflectance (ATR). The MOF-based catalyst samples were scanned from 4000 $cm^{-1}$ to 400 $cm^{-1}$ with a spectral resolution of 4 $cm^{-1}$ and 16 scans. The C-UiO-66 supported catalyst samples were prepared on a glass slide and placed under the objective lens microscope of a confocal Raman microscopy system. The Raman analysis was conducted in the 100–4000 $cm^{-1}$ spectral range using a Witec alpha 300R (WITec, GmbH, Ulm, Germany) equipped with 532 nm excitation laser. The measurements were captured using a 100× objective lens with an integration time of 5.07 s and a 50 mW laser power, with 10 accumulations. Crystallinity phase of the prepared catalysts was investigated with a powder X-ray diffractometer using a Rigaku SmartLab XRD equipped with Hypix-400 monochromatic CuKα ($\lambda$ = 1.506 Å) which diffracted in the range of 5° to 80° within a step size of 5° $min^{-1}$. The XRD signals were analysed and matched with Cambridge Crystallographic Data Center (CCDC) and Rigaku library. The surface composition and the chemical state of the series of catalysts were determined using X-ray photoelecton spectroscopy (XPS). Photoelectron spectra were recorded with a PHOIBOS 150 MCD 9 analyser from SPECS and a monochromatic AlK$\alpha$ X-ray energy of 1486.60 eV under vacuum conditions (10–9 mbar) and 25°C. The relative quantification of Ni, C, O and Zr was carried out using casa XPS

software. Binding energy was corrected to C1s at 284.5 eV. The thermal degradation phase analysis and stability were conducted using a PerkinElmer Pyris Diamond. The catalysts were decomposed from 30°C to 1000°C at a 10°C $min^{-1}$ heating rate with continuous flow of 50 ml $min^{-1}$ of $N_2$. The surface textural properties of the degassed C-UiO-66 catalysts were performed under nitrogen cryogenic temperature using a Micromeritic ASAP-2020. The C-UiO-66 and C-UiO-66@Ni surface morphology and microscopic structure were examined under ×100 000 magnification power using field emission scanning electron microscopy (FESEM) with a Novananosem-2300. All the samples were precoated with platinum using a JFT-1600, JEQL sputter coater. A field emission electron microscope (HRFESEM), brand: ZEISS, model: GeminiSEM 50, was used for mapping. The elemental compositions of the MOF were studied using EDX (Oxford Instruments Max 20). The acidity–basicity strength (TPD-$NH_3$/$CO_2$) of the synthesized catalysts was measured using a Micromeritics AutoChemII 2920 chemisorption analyser equipped with thermal conductivity detector (TCD). Sample pretreatment was conducted by heating 50 mg of powder catalyst at 150°C for 1 h under helium gas continuous flow of 30 ml $min^{-1}$. Then, the pretreated catalyst was probed with 10% $NH_3$ or 10% $CO_2$ at a flow rate of 10 ml $min^{-1}$ at 50°C within 30 min. The analysis temperature increased by 10°C $min^{-1}$ from 50°C to 800°C for the adsorption–desorption of the $NH_3$ and $CO_2$, respectively. The results of the catalyst acidity–basicity profiles were shown in curve form.

## 2.4. Deoxygenation reaction

Catalytic deoxygenation conversion of PFAD into green diesel was carried out in a semi-batch reactor with container capacity of 100 ml to contain 10 g of PFAD and 3 wt% of UiO-66 based catalyst. The reaction mixture was initially purged with $N_2$ for 10 min for the removal of air and $O_2$. Then, the reaction started by heating up to 320°C with fixed $N_2$ flow (20 ml $min^{-1}$) and steady stirring at 500 r.p.m. for 3 h. A study by Safa *et al.* mentioned that rich free fatty acid sample (table 1) requires high heat energy more than 320°C for the conversion of hydrocarbon through C–O and C–C cleavage mechanisms to occur for hydrocarbon formation [32]. The volatile hydrocarbons from the reaction were condensed in a flask collector connected to an external cooling water condenser (19°C). The catalytic deoxygenation reactions were determined by the RSM-CCD method. The eluted hydrocarbon aliquots were analysed using gas chromatography with a flame ionization detector (GC-FID) and further analysis with FTIR. The used MOF catalyst was separated from products and further washed with *n*-hexane for organic compound removal and oven dried at 105°C for 12 h for detailed characterization.

## 2.5. Response surface methodology–central composite design of palm fatty acid distillate deoxygenation reaction

This study, PFAD conversion into green diesel hydrocarbon via catalytic deoxygenation was performed using RSM generated by Minitab Statistical Software (version 21). The RSM was designed based on 5-level-3-factor of CCD to study the catalytic deoxygenation performances of C-UiO-66@Ni-20wt%. Three reaction variables were reaction time (1–5 h), catalyst loading (1–5 wt%) and reaction temperature at 20°C intervals, from 260 to 340°C. A complete design of catalytic deoxygenation reactions and a total of 20 experiments are depicted in tables 2 and 3, respectively.

## 2.6. Biofuel analysis

The liquid biofuel product analysis is carried out by GC-FID equipped with an HP-5 capillary column (5% phenyl methyl siloxane, 30 mm × 0.32 mm × 0.25 um, Agilent J&W). The alkane standard solution C8–C20 (99%, Sigma-Aldrich) was utilized as a reference standard for this analysis. Approximately 5 to 20 µl of liquid biofuels were dissolved with 1.5 ml *n*-hexane (98%, R&M); 1 µl of diluted biofuels was injected into GC with split ratio of 100. The injector temperature was programmed at 250°C, while the oven initial temperature was set at 40°C and idle for 6 min before heating up to 300°C with an increment of rate of 7°C $min^{-1}$. The injected aliquot was carried by $H_2$ at a flowrate of 30 ml $min^{-1}$. The elution of alkane components was determined according to retention time of the standard alkane mixture C8–C20 and the yield and selectivity are calculated using the following equations (2.1) and (2.2):

**Table 2.** Reaction variables and experimental level.

| variable | variables | level | | | | |
|---|---|---|---|---|---|---|
| | | −2 | −1 | 0 | 1 | 2 |
| *A* | time (h) | 1 | 2 | 3 | 4 | 5 |
| *B* | catalyst loading (wt%) | 1 | 2 | 3 | 4 | 5 |
| *C* | temperature (°C) | 260 | 280 | 300 | 320 | 340 |

**Table 3.** Experimental design generated by RSM and responses from each reaction.

| run order | Pt type | time (h) | catalyst loading (wt%) | temperature (°C) | experimental yield (%) | predicted yield (%) |
|---|---|---|---|---|---|---|
| 1 | 1 | 4 | 4 | 280 | 62.48 | 62.41 |
| 2 | 0 | 3 | 3 | 300 | 67.45 | 68.19 |
| 3 | 1 | 4 | 2 | 320 | 73.38 | 73.46 |
| 4 | 1 | 4 | 2 | 280 | 58.86 | 59.28 |
| 5 | −1 | 3 | 5 | 300 | 65.79 | 66.13 |
| 6 | −1 | 3 | 1 | 300 | 60.57 | 60.53 |
| 7 | 0 | 3 | 3 | 300 | 68.53 | 68.19 |
| 8 | 1 | 2 | 2 | 320 | 70.22 | 69.99 |
| 9 | 0 | 3 | 3 | 300 | 67.95 | 68.19 |
| 10 | 1 | 2 | 4 | 280 | 56.05 | 55.66 |
| 11 | −1 | 5 | 3 | 300 | 66.51 | 66.05 |
| 12 | 1 | 2 | 4 | 320 | 73.18 | 72.46 |
| 13 | −1 | 3 | 3 | 340 | 87.05 | 85.94 |
| 14 | 0 | 3 | 3 | 300 | 68.45 | 68.19 |
| 15 | 1 | 4 | 4 | 320 | 75.09 | 75.28 |
| 16 | −1 | 1 | 3 | 300 | 55.06 | 55.83 |
| 17 | 0 | 3 | 3 | 300 | 68.95 | 68.26 |
| 18 | −1 | 3 | 3 | 260 | 52.15 | 52.26 |
| 19 | 1 | 2 | 2 | 280 | 52.37 | 51.88 |
| 20 | 0 | 3 | 3 | 300 | 68.52 | 68.19 |

$$\text{Yield} = \frac{\sum n_o + \sum n_b}{\sum n_t} \times 100, \tag{2.1}$$

where $n_o$ = alkene peak area, $n_b$ = alkane peak area, $n_t$ = total peak area of eluted biofuel,

$$\text{Selectivity} = \frac{C_x}{\sum n_t} \times 100, \tag{2.2}$$

where $C_x$ = area of gasoline (C8–C9)/jet (C10–C16)/diesel (C17–C20), $n_t$ = total peak area of eluted biofuel.

## 2.7. Catalyst reusability and characterization analysis

Catalytic deoxygenation using C-UiO-66@NiO-20wt% was optimized using RSM-suggested optimum conditions of 3.14 h, 3.28 wt% of catalyst and 340°C reaction temperature for eight reusability reactions. The catalyst was recovered by filtration and washed with *n*-hexane to remove the reactants and

hydrocarbons from the catalyst surface. Pre-washed reused catalyst was oven-dried at 105°C for 6 h and reused for catalysing the deoxygenation of PFAD and so on for eight successive runs.

# 3. Results and discussion

## 3.1. Catalyst preparation

### 3.1.1. Functional group analysis

The infrared absorption spectra of synthesized Zr-MOF are shown in figure 1. The absorption spectra of parent C-UiO-66 are still existing in all hybrid C-UiO-66@Ni samples, thus evidencing that no chemical interaction and bonding formation between Ni–O and the skeleton structure of UiO-66 exist upon the deposition of different Ni weight percent. Similarly, Li *et al.* found that their modified Ni-UiO-66 sample exhibited no Ni-related infrared absorption peaks [33], which aligns with the findings of this study [33]. The broad absorption bands at 3700 $cm^{-1}$ to 2900 $cm^{-1}$ are related to the physisorption of –OH group from water molecule [34]. A low-intensity absorption band of UiO-66 centred at 1704 $cm^{-1}$ was assigned to C=O asymmetric stretch of residual DMF adsorbed on the framework [35]. The strong absorption bands centred at 1565 $cm^{-1}$ and 1391 $cm^{-1}$ are due to asymmetric and symmetric stretching vibrations of O–C–O which act as interconnection between $Zr^{4+}$ and –COOH [36]. A weak vibration band at 1504 $cm^{-1}$ is related to C=C of phenyl ring group [37,38]. Bands at lower absorption frequencies of 740 $cm^{-1}$, 662 $cm^{-1}$, 538 $cm^{-1}$ and 477 $cm^{-1}$ are associated with stretching vibration of Zr–O bonding within the C-UiO-66 framework [39]. As previously stated, there are no changes in the absorption peaks for the hybrid C-UiO-66@Ni samples upon the deposition of Ni–O implying that the loaded material did not alter the original structure of UiO-66.

### 3.1.2. Raman spectroscopy analysis

The C-UiO-66 and its derived catalysts are further characterized using a Raman spectrophotometer as a complementary analysis to support infrared data especially to determine the non-IR active vibration functional groups, as shown in figure 2. The vibration bands at 1615 $cm^{-1}$ and 1141–1136 $cm^{-1}$ are attributed to the C=C stretching mode of benzene ring of terephthalic acid [40]. The absorption bands at 1560 $cm^{-1}$ and 1449–1444 $cm^{-1}$/1427 $cm^{-1}$ are attributed to the C–C stretching vibrations of carboxylic group and asymmetric/symmetric O–C–O bending mode, present in the terephthalic acid linkers, respectively [41]. The absorption bands at 1301–1295 $cm^{-1}$ and 1615 $cm^{-1}$ are assigned to the D-band ($C_{edge}$–O/$C_{edge}$=O) and G-band (C=C) [22], respectively, as depicted in the zoomed graph of figure 2b. Absorption bands at 633 $cm^{-1}$ and 861 $cm^{-1}$ are related to C–H out of plane vibration bending of terephthalic links [42]. Absorption peaks at 513 $cm^{-1}$ and 430 $cm^{-1}$ represent the stretching of Zr–O–C and Zr–O [43], respectively. The bands shifting towards slightly higher wavenumbers from 1136 $cm^{-1}$ to 1141 $cm^{-1}$, 1295 $cm^{-1}$ to 1301 $cm^{-1}$, 1444 $cm^{-1}$ to 1449 $cm^{-1}$ upon the impregnation of Ni on C-UiO-66 are attributed to the shorter bond length molecule transition of C=C, C–O/C=O and O–C–O [44]. These phenomena could be related by measuring the D-band to G-band intensity ratio (refer to table 4) which revealed that upon Ni impregnation, the $I(D)/I(G)$ ratio increased from 0.72 to 0.93, indicating the formation of more MOF disordered structures with higher number of defects as the Ni percentage increased on C-UiO-66, similar to findings reported by Chen *et al.* [45]. The crystalline length ($L_a$) of the polyaromatic unit in MOF samples is calculated using the Tuinstra–Koenig relation [46] (equation (3.1)), giving the values of 26.62 nm, 22.53 nm, 21.75 nm and 20.69 nm for C-UiO-66, C-UiO-66@Ni-15wt%, C-UiO-66@Ni-20wt% and C-UiO-66@Ni-25wt%, respectively. These crystallite lengths are lower in the presence of Ni proving that the impregnation was successfully achieved, as evidenced by a decrease in crystallite length compared with undoped C-UiO-66 catalyst.

$$L_a = \frac{2.4 \times 10^{-10} \times (\lambda)^4}{I(D)/I(G)}, \tag{3.1}$$

where $L_a$ is crystalline length, $\lambda$ is excitation wavelength of the Raman laser (532 nm), and $I(D)/I(G)$ is the intensity ratio of D-band and G-band.

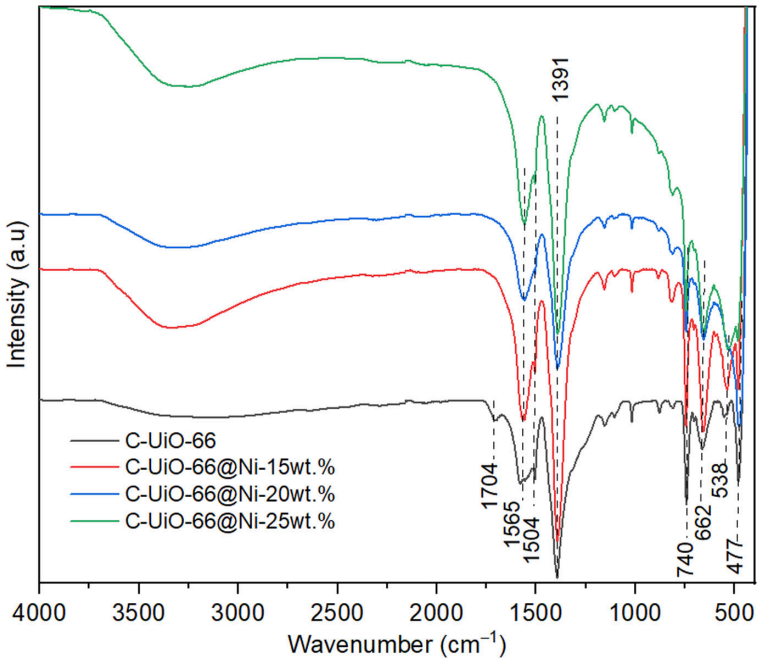


**Figure 1.** Infrared functional group identification for UiO-66 and hybrid UiO-66@NiO.

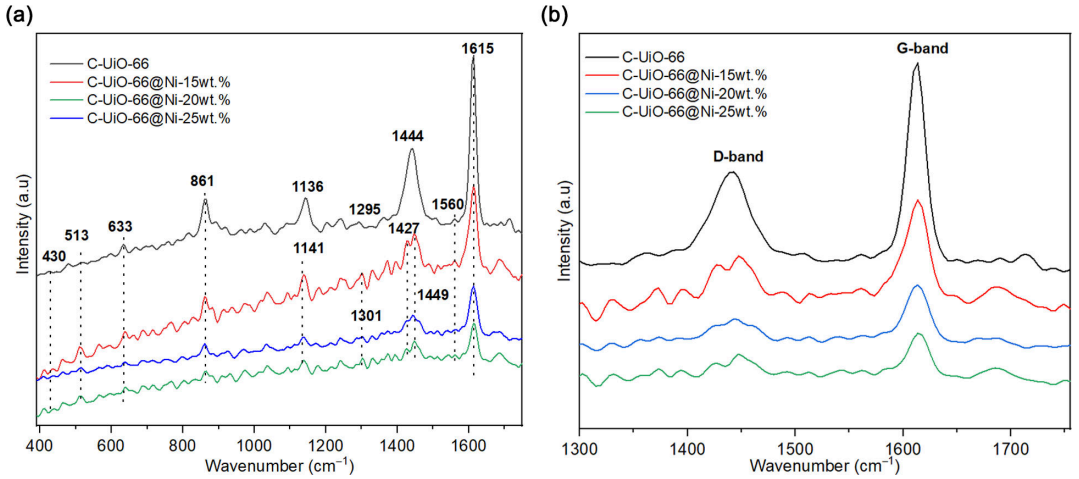


**Figure 2.** (a) Raman spectra of C-UiO-66 catalysts. (b) C-UiO-66 catalysts' D-band and G-band intensity comparison.

**Table 4.** Intensity ratio and crystalline length of synthesized catalysts.

| catalyst | intensity ratio, $I(D)/I(G)$ | crystalline length, $L_a$ (nm) |
|---|---|---|
| C-UiO-66 | 0.72 | 26.62 |
| C-UiO-66@Ni-15wt% | 0.85 | 22.53 |
| C-UiO-66@Ni-20wt% | 0.88 | 21.75 |
| C-UiO-66@Ni-25wt.% | 0.93 | 20.69 |

### 3.1.3. Crystallinity analysis

The X-ray diffraction profile of as-synthesized C-UiO-66 and C-UiO-66@Ni catalysts are included in figure 3. The XRD pattern of C-UiO-66 in this current work matches the pattern of simulated UiO-66 confirming the successful formation of MOF material, with the characteristic signals and crystal planes presented at $2\theta$ = 7.3° (111), 8.5° (200) and 25.7° (600). After incorporating Ni nanoparticles on C-UiO-66 surfaces via impregnation technique, the hybrid MOF diffraction profiles for C-UiO-66@Ni

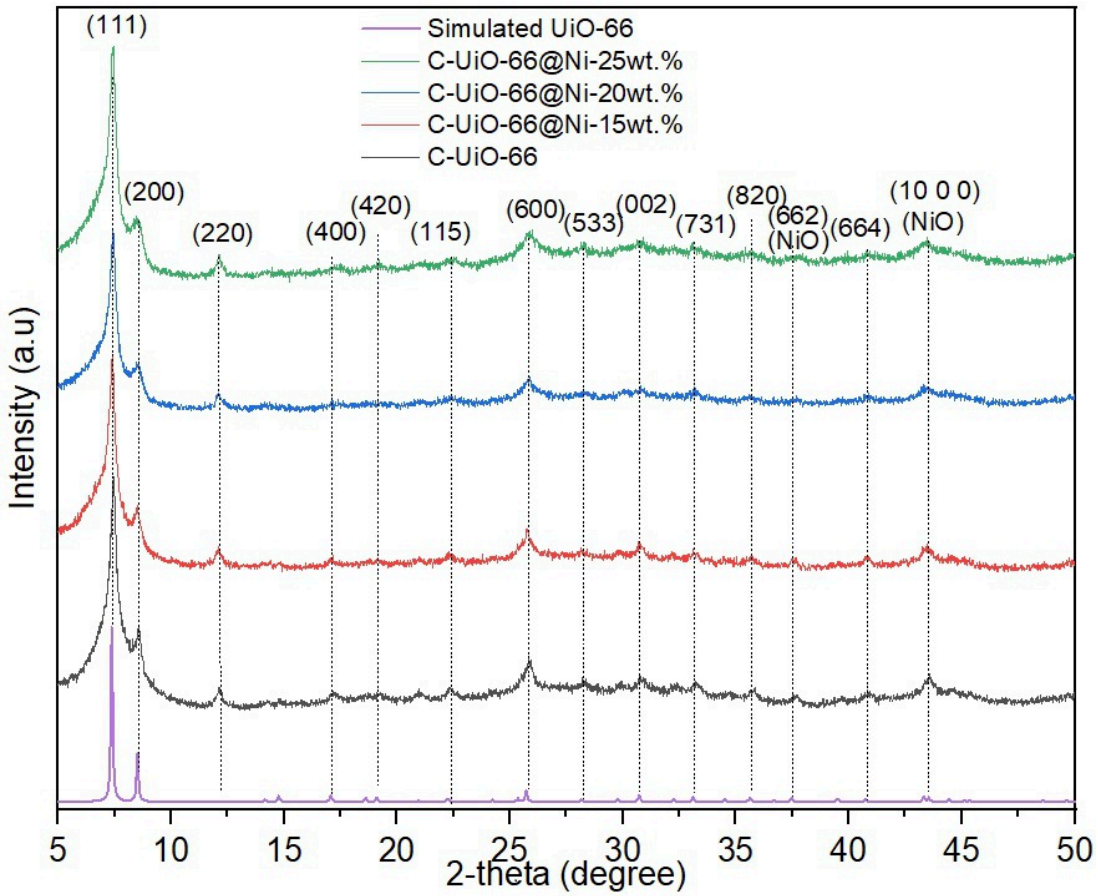


**Figure 3.** X-ray diffraction analysis of C-UiO-66 and hybrid C-UiO-66@Ni catalysts.

are showing a similar trend to the parent UiO-66 given that the XRD signals overlap each other. This shows that the matrix and crystallinity of C-UiO-66 are retained upon the dispersion of Ni nanoparticles as per discussed by Cai *et al.* [47]. Additional diffraction signals corresponding to Ni species are hardly distinguished due to the nano-sized particles distributed within the C-UiO-66 skeleton framework [48]. However, the NiO phases impregnated on UiO-66 precursor exhibited diffraction signals at $2\theta = 37.7°$ and 43.3°, consistent with JCPDS 00-047-104 pattern as reported by Thai *et al.* [49] and these signals overlapped with those of UiO-66.

### 3.1.4. X-ray photoelectron spectroscopy analysis

Survey scan in electronic supplementary material, figure S1, and figure 4a–d display the surface chemical state and electronic state of the constituent elements of the synthesized C-UiO-66 and C-UiO-66@Ni catalysts, as characterized by XPS, which confirms the presence of O, C and Zr. In addition to O1s, C1s and Zr3d spectra, the appearance of Ni2p signal for the C-UiO-66@Ni catalyst composite further confirms successful impregnation of Ni into C-UiO-66. The C1s spectra of the catalysts (refer to figure 4a) were deconvoluted into two peaks with binding energies approximately centred at 284.5 eV and 288.4 eV, which correspond to $sp^2$ C=C and oxygenated $sp^2$ carbon (i.e. C=O) [50,51], respectively. An additional third deconvoluted peak in samples with intermediate Ni contents (C-UiO66@Ni-15wt% and C-UiO-66@Ni-20wt%) was recorded at 286.3 eV and relates to carbon atoms singly bonded to oxygen atoms (C–O) [42]. Figure 4b shows the deconvolution signals of O1s at 531.5 eV, 530.1 eV and 533.0 eV, which were attributed to terephthalic acid of C=O, Zr–O and O=C–OH, respectively [49]. The deconvoluted Zr3d peaks of C-UiO-66 in figure 4c exhibit a doublet-fitted profile, characterized by binding energy of 182.6 eV ($Zr3d_{5/2}$) and 184.9 eV ($Zr3d_{3/2}$) with an energy difference of 2.3 eV, indicative of contribution of $ZrO_2$ [42]. Similarly, Zr3d spin-orbit doublet peak position for Ni-15% (C-UiO-66@Ni-15wt%) demonstrated no appreciable changes in the binding energy with respect to the undoped sample.

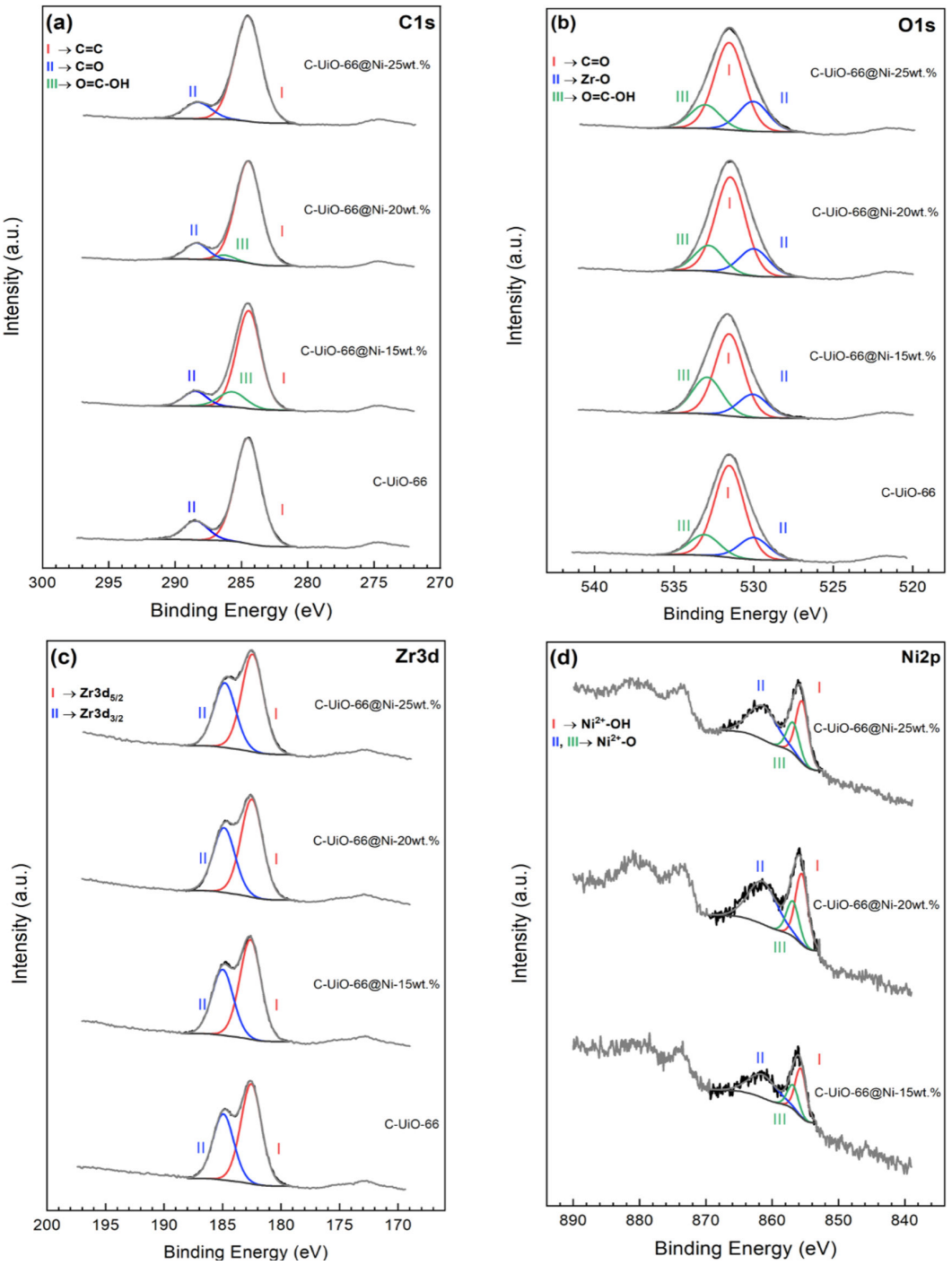


**Figure 4.** XPS spectra of synthesized C-UiO-66 and hybrid C-UiO-66@Ni: (a) C1s, (b) O1s, (c) Zr3d, (d) Ni2p.

However, the binding energy of the Zr3d spin-orbit doublet peak shifted towards slightly lower energy after increasing the amount of Ni (C-UiO-66@Ni-20wt%: $Zr3d_{5/2}$ =182.5 eV, $Zr3d_{3/2}$= 184.8 eV; and C-UiO-66@Ni-25wt%: $Zr3d_{5/2}$ =182.4 eV, $Zr3d_{3/2}$= 184.8 eV) due to electron transfer from Ni ions to Zr ions upon $Ni^{2+}$ doping, which leads to an increase in the electron cloud density around Zr [52]. Figure 4d presents the high-resolution Ni2p spectrum. The binding energy signals located at 855.6 eV and 856.7 eV correspond to the characteristic peaks of $Ni2p_{3/2}$ which are attributed to Ni–OH [30] and Ni–O [45] species, respectively. The presence of these two peaks is confirming the successful formation of NiO phases [53] in the C-UiO-66 sample. Additionally, a satellite peak is observed at 861.6 eV [54] alongside the main peaks attributed to a shake-up process [30]. The oxidation states and electronic properties of surface atomic species also provide information related to catalyst acidity and basicity profiles [55]. The metal species Zr and Ni were identified as Lewis acid sites due to their electron

deficiency [56] as corroborated by their XPS spectra. In addition, the surface acidity of synthesized catalysts was improved by the incorporation of $Ni^{2+}$ into UiO-66, as indicated by a slight shift in the $Zr3d_{5/2}$ binding energy with increasing Ni doping. Meanwhile, hydroxyl groups associated with carboxylate moieties (O=C–OH) observed at O1s binding energy of 533.0 eV were characterized as Brønsted acid sites as they easily undergo protonation and deprotonation forming metal-coordination bond [57]. According to Lee *et al.*, the electron-rich state of oxygen species was detected at lower O1s binding energies of 530.1 eV and 531.5 eV, attributed to strong Lewis base sites [58]. The acid–base profiles owing to the synthesized catalysts significantly influenced their catalytic performances specially during proton transfer and electron-donating mechanisms. Hence, the degrees of total acidity and basicity were further investigated via thermal probe desorption analys.

### 3.1.5. Thermal degradation behaviour analysis

The thermal degradation analyses were carried out to study the stability of C-UiO-66 and hybrid C-UiO-66@Ni catalysts as shown in TGA curves of figure 5. The graphs displayed three distinct degradation stages of weight loss in the range of 30–100°C, 119–200°C and 350–550°C. The first weight loss is identified as the evaporation of adsorbed water molecules and ethanol from the MOF surface cavities [59] with given loss amounts of 16.42%, 18.51%, 10.03% and 11.32% of C-UiO-66, C-UiO-66@Ni-15wt%, C-UiO-66@Ni-20wt% and C-UiO-66@Ni-25wt%, respectively. The second weight loss stage at temperature up to 200°C corresponded to decomposition of modulator and DMF trapped within MOF structure [60]. Next degradation temperature from 330°C to 580°C is determined as the breakdown of framework structure into $ZrO_2$ and organic linkers (terephthalic acid) accompanied with the decomposition of NiO [42] recorded at 33.64%, 38.18%, 43.72% and 46.25% for each the specimens C-UiO-66, C-UiO-66@Ni-15wt%, C-UiO-66@Ni-20wt% and C-UiO-66@Ni-25wt%, correspondingly. The catalyst stability is finalized up to 800°C as almost no weight loss is recorded.

### 3.1.6. Surface textural property analysis

The nitrogen adsorption isotherms at −196.15°C and BJH pore size distribution of the C-UiO-66 and hybrid C-UiO-66@Ni catalysts are featured in figure 6 and the numerical values presented in table 5. The synthesized materials exhibited hysteresis loops of type-IV isotherms confirming the MOF's mesoporous nature [61]. Evidently, the hysteresis loops of these MOF meso-structures are classified as H3-type parallel plate shaped pores as discovered on MOF's wide distribution pores [62]. In accordance with $N_2$ sorption analysis, the specific surface area of C-UiO-66 is measured at 670.11 $m^2\,g^{-1}$, while the hybrid C-UiO-66 impregnated with 15, 20 and 25 wt% of Ni are recorded at 554.17, 528.17 and 477 $m^2\,g^{-1}$, respectively. On further investigation using the BJH technique, the prepared specimens revealed multimodal wide pore distribution curves where the diameter ranges from 2 nm to 40 nm with a mesoporous nature. The pore distributions are recorded at 6.44 nm and average of 3.67 nm for parent C-UiO-66 and hybrid C-UiO-66@Ni samples, respectively. The significant reduction of specific surface area and pore size confirmed the successful loading of Ni nanoparticles on C-UiO-66 pore surfaces. According to Tamjidi *et al.*, the mesoporous pore structures are significant for catalytic performance of green diesel production [34].

### 3.1.7. Microscopic morphology and elemental composition analysis

Micrograph images taken by FESEM analysis are depicted in figure 7 displaying the polygonal nanostructure of synthesized C-UiO-66 and hybrid C-UiO-66@Ni. The polygonal nanocrystal structure was maintained upon the Ni deposition because there was no chemical interaction between these two species that would significantly modify the framework structures. However, particle agglomeration was clearly evident with the increase of Ni impregnation weight percent causing a slight formation of irregular shape on the crystallite structure. This finding is further supported by XRD analysis, which reveals that the intensity of the MOF signals decreases as the percentage of Ni deposition increases. This decrease in intensity suggests that the Ni species are masking the surface of the precursor framework, thereby reducing the crystallinity of the MOF. Despite the lack of a clear XRD diffraction pattern from the Ni species, the incorporation on MOF surface is sufficient to modify the framework's diffraction characteristics. This is further confirmed by the elemental analysis, which was performed using EDX to investigate the composition of C-UiO-66 and C-UiO-66@Ni. The results,

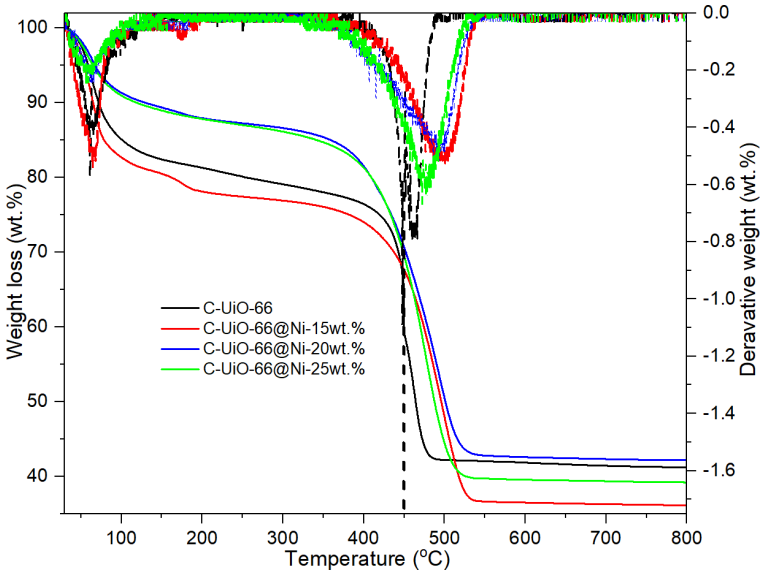


**Figure 5.** Thermal decomposition curves of synthesized UiO-66 and hybrid UiO-66@NiO catalysts.

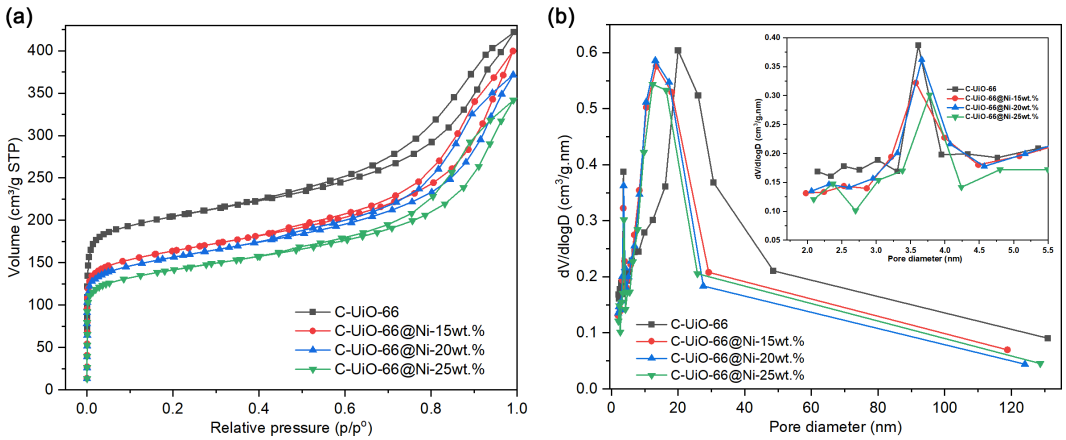


**Figure 6.** (a) $N_2$ sorption isotherms of UiO-66 and hybrid UiO-66@NiO catalysts. (b) BJH pore size distribution analysis.

**Table 5.** The $N_2$ sorption and $CO_2$, $NH_3$ adsorption analysis results.

| catalyst | specific surface area ($m^2\ g^{-1}$) | pore volume ($cm^3\ g^{-1}$) | average pore diameter (nm) | total basicity (mmol $g^{-1}$) | total acidity (mmol $g^{-1}$) |
|---|---|---|---|---|---|
| C-UiO-66 | 670.11 | 0.45 | 6.44 | 0.92 | 2.67 |
| C-UiO-66@Ni-15wt% | 554.17 | 0.45 | 3.58 | 1.26 | 4.10 |
| C-UiO-66@Ni-20wt% | 528.17 | 0.41 | 3.66 | 1.34 | 4.58 |
| C-UiO-66@Ni-25wt% | 477.30 | 0.38 | 3.77 | 1.53 | 4.77 |

summarized in table 6, confirm the existence of C, O, Zr and impregnated Ni in the synthesized framework. Moreover, the mapping images, in electronic supplementary material, figure S2, reveal a uniform and high-density distribution of elements, indicating a strong interaction between the active metal (Ni) and the catalyst precursor (C-UiO-66). This strong interaction is likely responsible for the altered diffraction characteristics observed in the XRD analysis, suggesting that the Ni species are indeed integrated into the MOF framework. According to Shin *et al.*, the uniform dispersion of active components on precursor structures leads to the formation of highly porous active sites, promoting the efficient catalytic deoxygenation of biofuels [20].

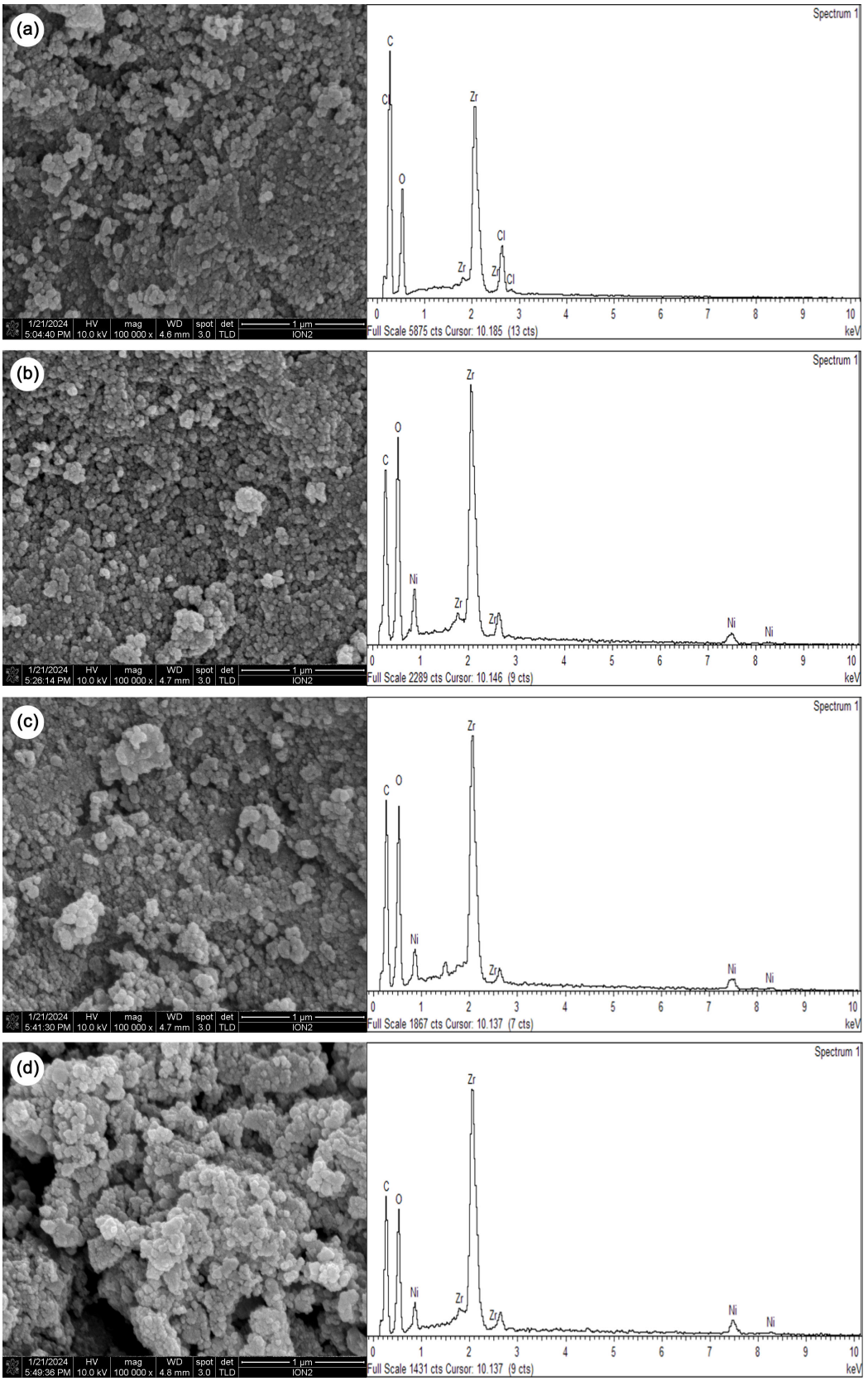


**Figure 7.** Microscopic morphologies under ×100 000 magnification power and EDX spectra of (a) C-UiO-66, (b) C-UiO-66@Ni-15wt%, (c) C-UiO-66@Ni-20wt%, (d) C-UiO-66@Ni-25wt%.

**Table 6.** Energy-dispersive X-ray scanning of the elemental percentage composition for C-UiO-66, C-UiO-66@Ni-15wt%, C-UiO-66@Ni-20wt% and C-UiO-66@Ni-25wt%.

| catalyst | element percentage (wt%) | | | |
|---|---|---|---|---|
| | C | O | Zr | Ni |
| C-UiO-66 | 45.31 | 24.64 | 30.05 | — |
| C-UiO-66@Ni-15wt% | 38.13 | 31.29 | 25.61 | 4.97 |
| C-UiO-66@Ni-20wt% | 40.95 | 28.40 | 25.41 | 5.51 |
| C-UiO-66@Ni-25wt% | 39.69 | 24.34 | 28.74 | 7.23 |

### 3.1.8. Acid–base chemisorption analysis

The acid and base profiles of synthesized C-UiO-66 supported catalysts were analysed using temperature programmed desorption as illustrated in figure 8 and table 5. The acid and base profiles are significantly involved in deoxygenation and cracking processes for which each active site is favourable for C–C bond cleavage and promotes the removal of carboxylic group through C–O bond scission [63], respectively. An excessive strength of acidity would promote coke formation and catalyst deactivation. Meanwhile, the basic sites could preserve the catalytic deoxygenation process by inhibiting the coke formation [64]. The acidity–basicity strength can be categorized depending on the desorption temperature of the probe gas ($NH_3$ and $CO_2$): weak active site (<200°C), medium active site (200–450°C) and strong active site (>450°C) [65]. These synthesized catalysts exhibited three major $NH_3$ desorption peaks of low, medium and strong acidic strength, attributed to Lewis and Brønsted acid sites [66], respectively. Total acidity value of C-UiO-66 is 2.57 mmol $g^{-1}$, and the desorption values increased after the Ni impregnation addressing the additional Lewis acidic site species. Referring to table 4, the increment of Ni loading (wt%) on the C-UiO-66 proportionally increasing the total acid value in the following order: C-UiO-66 < C-UiO-66@Ni-15wt% < C-UiO-66@Ni-20wt% < C-UiO-66@Ni-25wt%. According to Rezaei and Taghidazeh, the Lewis acid sites are attributed to the unsaturated Zr sites known as $(Zr_6O_4(OH)_4)^{12+}$, while the Brønsted acid sites are assigned to $OH/H_2O$ groups of C-UiO-66 node [37]. The TPD-$CO_2$ profile of C-UiO-66 showed a strong $CO_2$ desorption of 0.92 mmol $g^{-1}$, and the desorption significantly increased with the addition of moderate $CO_2$ desorption peak as Ni deposited on the UiO-66 support. The reported studies described that the metal–oxygen pair (Ni–O) associated with moderate basicity strength while the strong $CO_2$ desorption would happen on unsaturated oxygen atom basic sites [67]. The basicity profiles demonstrated that the basicity strength increases with the amount of Ni with the basicity strength in the following order: C-UiO-66@Ni-25wt% > C-UiO-66@Ni-20wt% > C-UiO-66@Ni-15wt% > C-UiO-66. The synergy between metal sites and C-UiO-66 support which provides acidic and basic properties could be responsible for obtaining the excellent catalytic deoxygenation activities.

## 3.2. Screening activities for the catalyst optimization selection

Figure 9 presents the screening results of deoxygenated PFAD hydrocarbon yields with specific product fractions performed at a consistent temperature of 320°C for 3 h in inert $N_2$ flow facilitated by catalysts and without catalyst. Alkane and alkene mixtures (C8–C17) were identified by GC-FID as deoxygenated liquid products of green diesel. Referring to table 1, palmitic acid (C16) and oleic acid (C18:1) were the major PFAD compositions, resulting in large fractions of C15 and C17 hydrocarbon products. Theoretically, the deoxygenation reaction removes the fatty acid's oxygenated carbon species of carboxyl and carbonyl groups, releasing carbon dioxide and water as byproducts. Consequently, the produced hydrocarbons losing one carbon chain from the parent fatty acid for instance C15 (pentadecane and pentadecene) and C17 (heptadecane and heptadecene) derived from palmitic and oleic acid [10], respectively. The presence of C-UiO-66 and its Ni-doped variants enhanced reaction rates and yields by providing active sites for fatty acid adsorption, lowering the activation energy and selectively transformed fatty acids into targeted hydrocarbons, and stabilized reaction intermediates [68]. The adsorption on catalyst active sites facilitated decarboxylation and decarbonylation of fatty acids, converting them into hydrocarbons with yields up to 76%, compared with only 21% without catalyst. Additionally, the incorporation of Ni into the catalyst precursor further enhanced the catalytic activity, particularly in facilitating the cracking of complex lipid chains into more valuable lighter

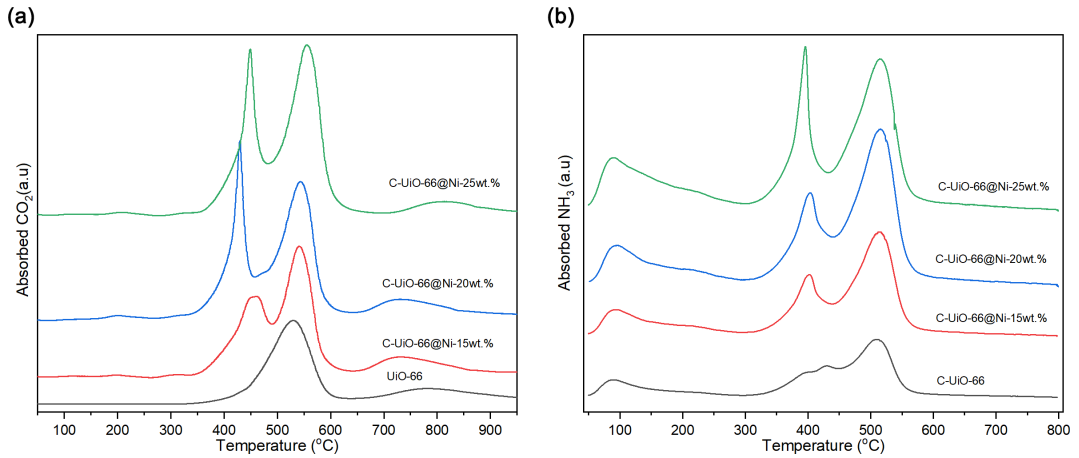


**Figure 8.** Temperature programmed chemisorption analysis: (a) adsorption–desorption of $CO_2$; (b) adsorption–desorption of $NH_3$.

products, owing to the abundant distribution of Lewis acid active sites [69]. Referring to figure 9, the order of catalytic deoxygenation reaction was C-UiO-66@Ni-25wt% > C-UiO-66@Ni-20wt% > C-UiO-66@Ni-15wt% > C-UiO-66 > blank.

The effective catalytic deoxygenation reaction of fatty acids into hydrocarbons was significantly attributed to the optimal acidity–basicity strength followed by the textural surface profile [70]. Specifically, Lewis acid sites' strong affinity towards oxygenated groups of fatty acids facilitated C–O activation and suppressing C–C bond cleavage resulting in deoxygenation pathway to generate straight-chain hydrocarbon formation [71]. Brønsted acid sites protonate the carboxylic groups, forming carbocation intermediates, which typically occur during the aromatization process [72]. Meanwhile, the basic sites were found to inhibit secondary cracking reactions that otherwise convert liquid hydrocarbons into lighter gaseous products, thereby reducing the overall liquid yield [73]. However, no significant yield difference was observed when catalysed by C-UiO-66@Ni-20wt% and C-UiO-66@Ni-25wt%, coinciding with that highly saturated active acid–base sites are slightly less efficient and will reduce the reactivity due to less porosity for the diffusion interaction between active sites and retreatant molecules towards product conversion [74]. Considering catalysis sustainability, C-UiO-66@Ni-20wt% was selected for deoxygenation optimization procedures since it provided appropriate surface area, porosity and acid–base properties.

## 3.3. Statistical analysis of regression model on hydrocarbon yield production

The catalytic optimization of deoxygenation reaction derived from PFAD was carried out using the RSM-CCD approach which involved 20 experimental runs to study the effect of single factors and the interaction among reaction factors in response to yield of hydrocarbon as summarized in table 3. In addition, the results of the analysis of variance (ANOVA) for the calculated regression model of catalytic deoxygenation reaction, which evaluates the significance level of the model statistically, model fitness and the interactions of reaction parameters (both individually and collectively), are summarized in table 7. Equation (3.2) represents the developed quadratic polynomial coefficient regression model, which describes the relationship of hydrocarbon yield as a response for the interaction between reaction variables in terms of coded factors of $A$, $B$ and $C$ that represent time, catalyst loading and temperature, respectively.

$$\begin{aligned}\text{Yield } (\%) = &-89.4 + 29.19A + 14.66B + 0.160C - 1.905A^2 - 1.306B^2 + 0.000747C^2 \\ &- 0.164AB - 0.0491AC - 0.0164BC\,. \end{aligned} \tag{3.2}$$

The AVOVA results and coefficient of determination ($R^2$ = 99.47%, $R^2$-adj= 99.00%) indicated that the model predictability for PFAD deoxygenation reaction is acceptable. The difference between both $R^2$ is small, 0.47%, indicating consistency between the model prediction and experimental data which can be evidently observed through a parity plot in figure 10a as actual values are strongly correlated and distributed uniformly close to the predicted values. The Fisher test ($F$-value) of the model yields a value of 210, and the corresponding $p$-value is less than 0.0001, which is well below the

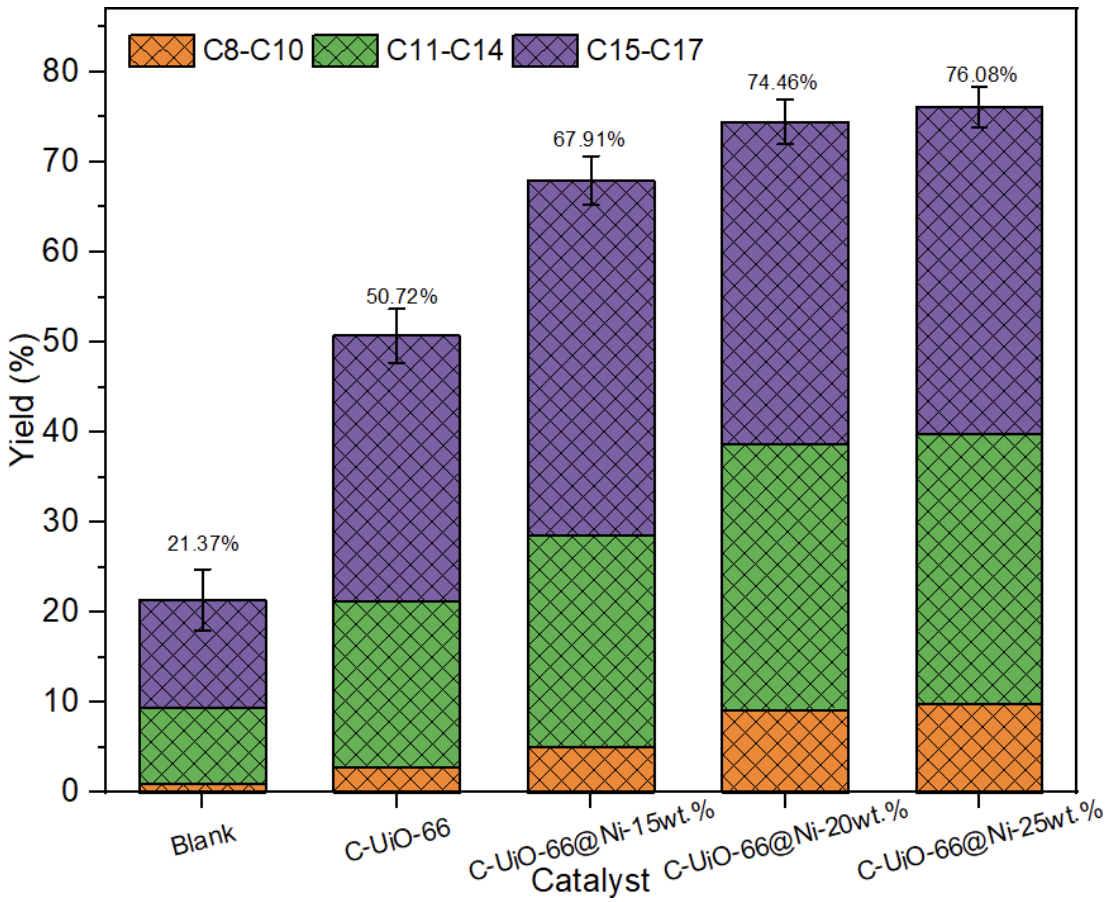


**Figure 9.** Catalytic deoxygenation screening carried out at 320°C for 3 h catalysed with 3 wt% of catalyst.

**Table 7.** Results of the regression model for full quadratic of deoxygenated hydrocarbon yield derived from PFAD.

| source | d.f. | adj SS | adj MS | *F*-value | *p*-value |
|---|---|---|---|---|---|
| model | 9 | 1365.04 | 151.67 | 210 | <0.0001 |
| linear | 3 | 1223.4 | 407.8 | 564.63 | <0.0001 |
| time (*A*) | 1 | 104.5 | 104.5 | 144.69 | <0.0001 |
| catalyst loading (*B*) | 1 | 31.39 | 31.39 | 43.46 | <0.0001 |
| temperature (*C*) | 1 | 1087.52 | 1087.52 | 1505.75 | <0.0001 |
| square | 3 | 132.86 | 44.29 | 61.32 | <0.0001 |
| time × time ($A^2$) | 1 | 91.23 | 91.23 | 126.32 | <0.0001 |
| catalyst loading × catalyst loading ($B^2$) | 1 | 42.89 | 42.89 | 59.39 | <0.0001 |
| temperature × temperature ($C^2$) | 1 | 2.25 | 2.25 | 3.11 | 0.108 |
| two-way interaction | 3 | 8.78 | 2.93 | 4.05 | 0.04 |
| time × catalyst loading (*AB*) | 1 | 0.21 | 0.21 | 0.3 | 0.598 |
| time × temperature (*AC*) | 1 | 7.7 | 7.7 | 10.67 | 0.008 |
| catalyst loading × temperature (*BC*) | 1 | 0.86 | 0.86 | 1.2 | 0.3 |
| error | 10 | 7.22 | 0.72 | | |
| lack-of-fit | 5 | 5.83 | 1.17 | 4.19 | 0.071 |
| pure error | 5 | 1.39 | 0.28 | | |
| total | 19 | 1372.27 | | | |

$S = 0.849$, $R^2 = 99.47\%$, $R^2$-adj = 99%, $R^2$(pred) = 96.32%

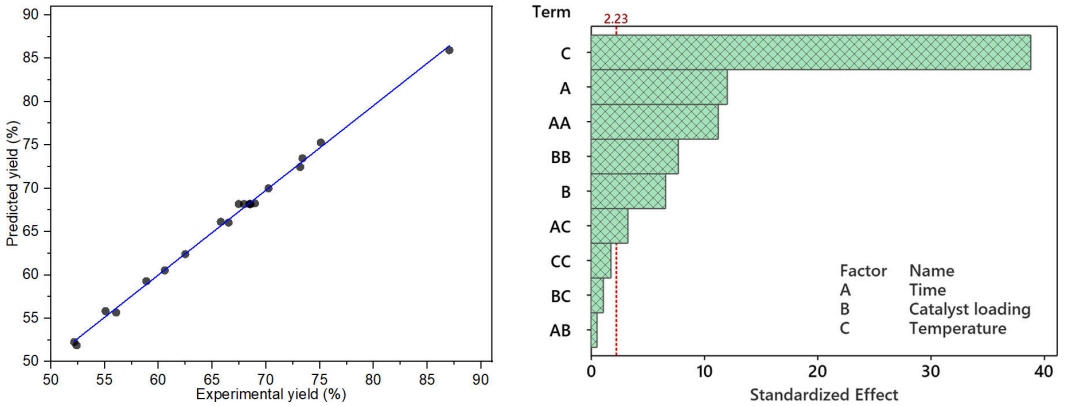


**Figure 10.** (a) Hydrocarbon yield comparison between prediction based on calculation and experimental tests. (b) Pareto chart of standardized independent variables in response of hydrocarbon yield set at significance level, $a = 0.05$.

significance threshold of 0.05, thereby confirming the relevance and statistical significance of the proposed quadratic polynomial model. Furthermore, the model's lack of fit recorded *p*-value of 0.071 and *F*-value of 4.19 to be non-significant which indicates that the responses are fitted for the proposed model. Besides relying on a *p*-value of less than 0.05 as an indicator of significance, the hierarchy of variables can be established from most to least significant based on the *F*-value. In this model, temperature (*C*) emerges as the most significant variable in the deoxygenation reaction, as evidenced by its highest *F*-value of 1505.75, a finding that is further corroborated by the Pareto chart. As shown in figure 10b, the sequence of significance of the factors affecting the reaction, from most to least significant, is determined to be $C > A > A^2 > B^2 > B > AC > C^2 > BC > AB$. The factors $C^2$, *AB* and *BC* are found to be non-significant variables, characterized by *p*-value greater than 0.05 and lower *F*-values, which suggest that those variables have least effect on the deoxygenation reaction.

## 3.4. Response surface methodology interaction of time, temperature and catalyst loading for deoxygenation of palm fatty acid distillate catalysed via C-UiO-66@Ni-20wt%

Figure 11a–c shows the surface three-dimensional plots for the interaction studies between reaction time (*A*), catalyst loading (*B*) and temperature (*C*), whereas the counter plots are reported in electronic supplementary material, figure S4. Figure 11a illustrates the interaction between reaction time and catalyst loading of PFAD deoxygenation reaction while keeping reaction temperature constant at 300°C. The increase of catalyst loading and reaction time enhanced biofuel yield by providing more active sites and sufficient duration for reactant adsorption and oxygen removal from fatty acids, resulting in refined hydrocarbon formation [75]. At higher catalyst loading, more acid–base active site distribution enables more effective and uniform catalytic decarboxylation and decarbonylation routes, reducing diffusion limitations and enhancing overall reaction reactivity [20]. Notably, the yield increased from 50% to over 65% with a proportional increment of catalyst loading from 1 to 5 wt%, within 1 to 4 h of reaction time. The excessive catalyst loading and extended reaction time reduced the liquid hydrocarbon yield to 50% due to excessive C–C cracking producing gaseous hydrocarbons and coke formation from polymerization side reactions, which consequently deactivated the catalyst [76].

Figure 11b shows the interaction of reaction time, *A* (1 to 5 h), and temperature, *C* (260 to 340°C), catalysed consistently with catalyst loading of 3 wt%. The three-dimensional plot demonstrated that longer reaction time with an increase reaction temperature led to high production of straight-chain hydrocarbons with yield > 80%. The higher reaction temperature provides more kinetic energy for the fatty acid molecules to achieve more effective collision and diffuse within the porous structure of the active sites, where they subsequently undergo a molecular structural rearrangement, losing their oxygenated components and transforming into hydrocarbons [75]. At a short reaction time less than 2 h, the catalytic reaction is not sufficiently effective to complete the transformation of fatty acids into hydrocarbon formation, thus resulting in lower yield < 80% though the reaction temperature is maximized.

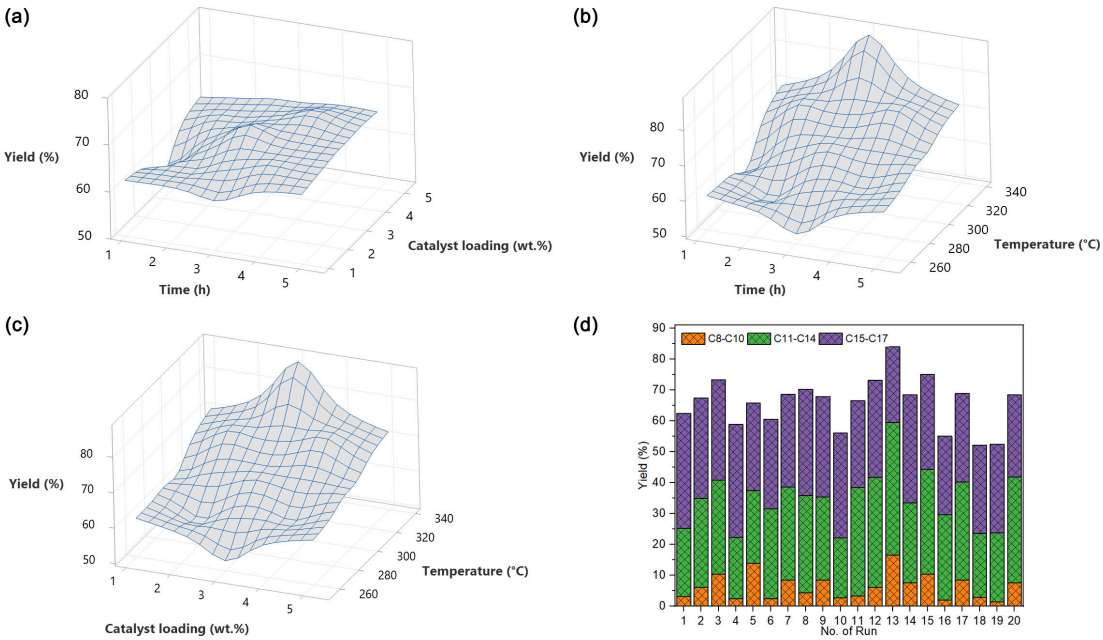


**Figure 11.** Optimization three-dimensional surface plots of hydrocarbon yield against reaction variable interactions: (a) time–catalyst loading, (b) time–temperature, (c) catalyst loading–temperature. (d) Hydrocarbon yield fraction based on experimental design reaction parameters.

Figure 11c illustrates the relationship between catalyst loading, *B*, and reaction temperature, *C*, in response to hydrocarbon synthesis with a fixed reaction time of 3 h. Simultaneous increment of catalyst loading and reaction temperature literally increases the reaction rate, where more active sites are provided for the fatty acid molecules to rapidly diffuse in and out from the catalyst and achieving effective collision with each other to generate more hydrocarbon yield [7,63]. However, in this reaction interaction, the yield is significantly influenced by a temperature from 260°C to 340°C resulting in more hydrocarbon production from 50% to more than 80% as catalysed at any catalyst loading ranging from 1 to 5 wt.%.

Figure 11d illustrates the hydrocarbon yield fractions categorized by carbon chain length, including C8–C10, C11–C14 and C15–C17, related to gasoline, kerosene and green diesel compositions [21,77], respectively. These yields, tied to the reaction conditions outlined in table 2, vary across different experimental runs. Experiment 13 achieved the highest hydrocarbon yield of 87.05%, whereas Experiment 18 recorded the lowest yield of 52.15%, despite both employing 3 wt% UiO-66@Ni-20wt% catalyst for 3 h at reaction temperatures of 340°C and 260°C, respectively. Although the distribution of acid–base active sites and the reaction time were kept constant, the reaction rates differed significantly because the amount of heat energy absorbed by the reactants influenced their diffusion over the active surfaces, leading to variations in effective molecular collisions and activation energy, consequently resulting in different hydrocarbon yields [78]. As the reaction temperature increased from 280°C to 340°C, the selectivity towards shorter hydrocarbon fractions (C8–C10 and C11–C14) increased from 2.9% and 20.73% to 16.53% and 42.89%, respectively, indicating that higher thermal conditions promote decarboxylation, decarbonylation and cracking pathways [79].

## 3.5. Response surface methodology model validation, reusability and catalyst deactivation analyses

After completing 20 experiments recommended by the CCD, the response surface optimization of reaction variables was generated to obtain the highest deoxygenated hydrocarbon yield in accordance with the fitted regression formula presented in equation (3.1). A total of 25 responses were provided, for which the criteria selection of optimized conditions was based on high desirability and relatively high yield over minimal reaction process. The response optimizer predicted the optimal reaction conditions to be 3.14 h, 3.28 wt% of catalyst loading and 340°C, which resulted in the highest predicted yield at 90.05% as highlighted in table 8. The reaction was conducted in triplicate applying the

**Table 8.** Optimum reaction variables recommended by optimizer prediction.

| factor | time (h) | catalyst loading (wt%) | temperature (°C) |
|---|---|---|---|
| high limit | 5 | 5 | 340 |
| optimized | 3.14 | 3.28 | 340 |
| low limit | 1 | 1 | 260 |
| optimizer prediction = 90.05% | 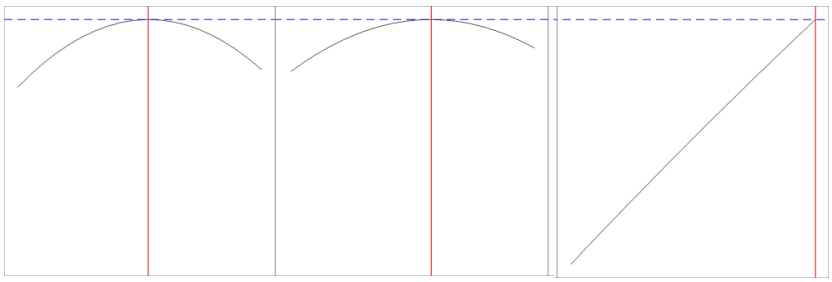 | | |

optimized parameter prediction, and the average yield was recorded at 87.65%, which is slightly lower than the targeted yield. A lower error rate of 2.67% was determined, indicating that the optimization reaction was well performed and achieved a higher hydrocarbon yield, as well as demonstrating the efficiency of the catalyst in catalysing the PFAD reaction [80].

Then, catalyst reusability tests of optimized conditions were carried out as the product yield shown in figure 12a. The catalytic reaction effectively catalysed and converted PFAD to high hydrocarbon yield up to 80% in the first three reuse runs, despite a depletion rate of 2–7% for consecutive uses. Upon eight consecutive usages of C-UiO-66@Ni-20wt%, the hydrocarbon yield decreased significantly to 30% due to catalyst deactivation, resulting in a less effective conversion of long-chain fatty acids into deoxygenated biofuel [15]. This deactivation is mainly attributed to reactants and residues/cokes that accumulated on the catalyst's active sites, which reduces the catalyst's acidity and basicity properties, subsequently hindering the catalytic deoxygenation reaction [81]. Figure 12b of physisorption analysis displays the reduction of $N_2$ adsorption–desorption hysteresis loop for the spent catalyst indicating a decrease in surface availability, consistent with a decrease in surface area from 528.17 to 311.52 $m^2\,g^{-1}$ upon eight consecutive reactions confirms the surface blockage, and is further supported by pore volume reduction from 0.41 to 0.26 $cm^3\,g^{-1}$ indicating the pore depth is being covered by contaminants. Figure 12d shows the microscopic morphology of fresh and spent C-UiO-66@Ni-20wt% catalysts at ×100 000 magnification, revealing a more packed and denser surface texture with larger particles embedded on the catalyst surface after repeat usage in contrast to the fresh catalyst (figure 12c).

The chemical properties of the spent C-UiO-66@Ni-20wt% catalyst were also characterized using techniques such as acid–base absorption and infrared spectroscopy, as shown in figure 12e–g, to investigate the chemical changes that occur upon catalyst deactivation. The chemisorption analysis, TPD-$CO_2$ and TPD-$NH_3$ results also demonstrated the lower adsorption intensity recorded at 0.56 and 1.21 mmol $g^{-1}$, respectively (table 9). As a result, the presence of residues (cokes, PFAD) that remain on the catalyst surface inhibits the probe gas from being completely adsorbed and interacting with active sites thus reducing basicity–acidity measurement which consequently reduces the catalytic reactivity and selectivity during the deoxygenation reaction [82]. The FTIR spectra of spent catalyst demonstrated additional absorption bands at 2976 $cm^{-1}$, 2825 $cm^{-1}$, 1681 $cm^{-1}$ and 1266 $cm^{-1}$ assigned to the symmetrical and asymmetrical aliphatic $–CH_2$ stretching [83, 84], –C–O of ether group [76] and $–CH_3$ bending [85], respectively, confirming the presence of fatty acids and biofuels on the catalyst surfaces. Nevertheless, other functional groups of organic linkers remained unchanged. Thus, the loss of active sites significantly affects the efficiency of catalytic deoxygenation, as it reduces the catalyst ability to adsorb and desorb for the conversion of fatty acids into hydrocarbons.

# 4. Conclusion

UiO-66 was successfully synthesized via a solvothermal method and was utilized as a catalyst precursor for the incorporation of Ni nanoparticles ($n$ = 15, 20 and 25 wt%). The catalyst was activated through partial carbonization at 300°C to enhance its thermal stability, improve the dispersion of Ni

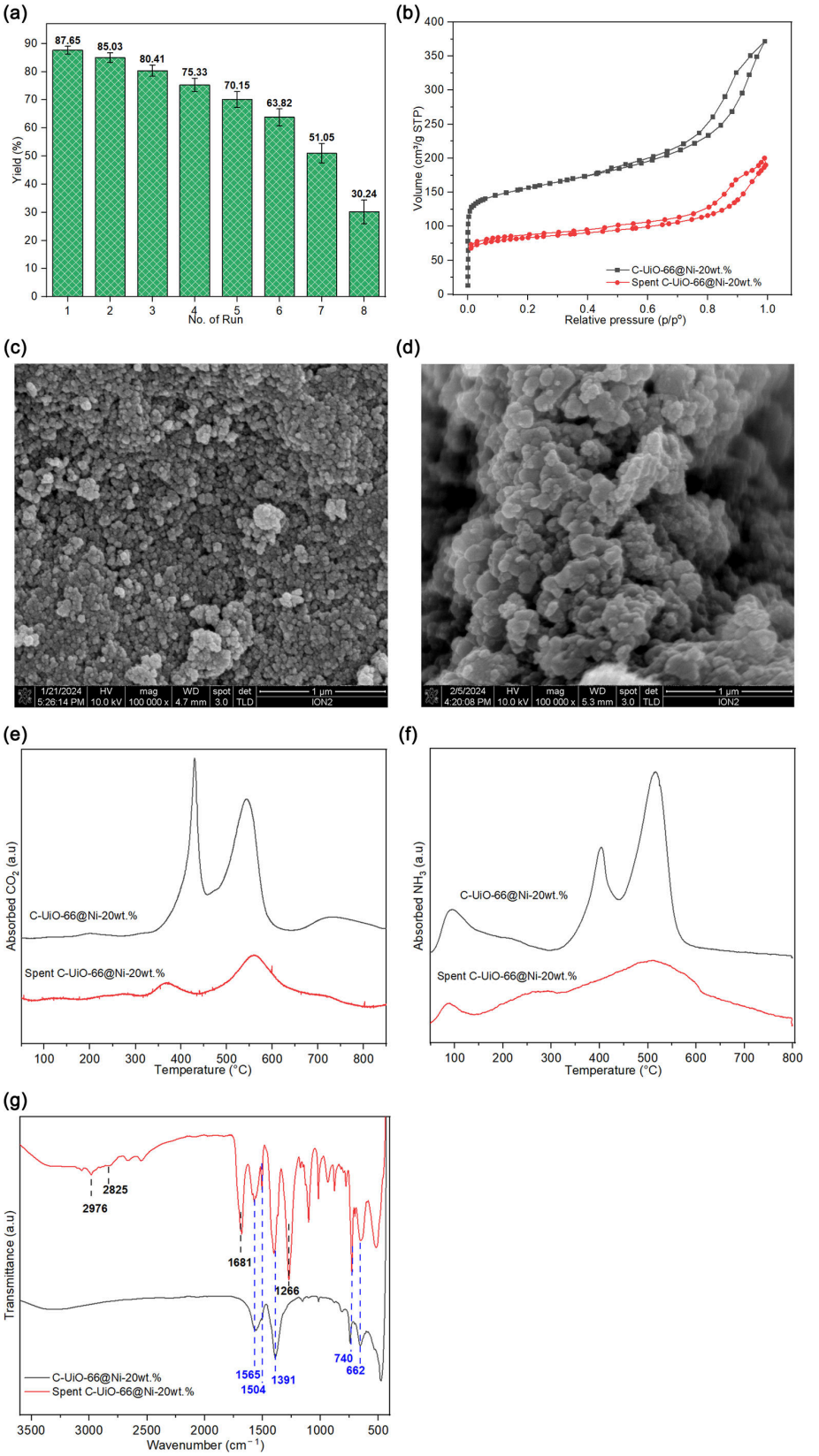


**Figure 12.** Reusability and deactivation analysis. (a) Reusability runs, (b) physisorption isotherm, (c) FESEM image of fresh catalyst, (d) FESEM image of spent catalyst, (e) TPD-$CO_2$, (f) TPD-$NH_3$, (g) FTIR spectra.

nanoparticles within the UiO-66 framework, and increase the number of catalytically active sites to facilitate the PFAD deoxygenation reaction. The XRD patterns of the synthesized catalysts matched those of pristine UiO-66, confirming that Ni incorporation and partial carbonization did not alter

**Table 9.** The physical and chemical analysis comparison of fresh and used C-UiO-66@NiO-20wt% catalyst.

| catalyst | surface area ($m^2$ $g^{-1}$) | pore volume ($cm^3$ $g^{-1}$) | pore diameter (nm) | total adsorption (mmol $g^{-1}$) | | yield (%) |
|---|---|---|---|---|---|---|
| | | | | $NH_3$ | $CO_2$ | |
| fresh | 528.17 | 0.41 | 3.66 | 4.58 | 1.34 | 82.4 |
| after eight uses | 311.52 | 0.26 | 3.34 | 1.21 | 0.56 | 30.1 |

the original MOF structure. Similar to infrared spectroscopy, no Ni-related absorption peaks were observed, indicating the absence of chemical bonding between Ni and the UiO-66 structure. EDX and XPS techniques were employed for elemental analysis, confirming the presence of well-dispersed Ni within polygonal nanostructure of C-UiO-66, with $Ni2p_{3/2}$ binding energies reported to be at 855.6 eV and 856.7 eV, thereby enhancing the catalytic performance for the conversion and selectivity. The C-UiO-66 and C-UiO-66@Ni catalysts exhibited large surface areas and adequate total acid–base properties to promote hydrocarbon conversion from fatty acids. In addition, these catalysts featured both Lewis acid and Brønsted acid sites, which were significantly involved in C–O scission and C–C cleavage reactions. C-UiO-66@Ni-20wt% was screened and subjected to response surface optimization (RSM) of PFAD hydrocarbon deoxygenation to study the interaction between reaction time, catalyst loading and reaction temperature. The regression determination, $R^2$, and $p$-value were 99.47% and >0.0001, respectively, indicating a high degree of agreement between the predicted and experimental yields. Validation of RSM model using optimized parameters (3.14 h, 3.28 wt% catalyst loading and 340°C reaction temperature) resulted in an 87.65% hydrocarbon yield. Catalyst reusability tests were performed by repeating the optimized deoxygenation reaction, during which the hydrocarbon yield gradually decreased by 2–7% until the seventh run and then significantly declined from 51.05% to 30.24% in the eighth cycle. Further characterization of the catalyst deactivation revealed that it was caused by the deposition of reactants that agglomerated on the active sites, as shown in the FESEM images and supported by the catalyst surface area and pore volume reduction. Infrared spectroscopy and acid–base density characterization also revealed a decrease in intensity, primarily due to the loss of the catalyst active sites. Overall, the MOF-based C-UiO-66@Ni catalyst exhibited better catalytic deoxygenation of PFAD at lower reaction temperatures (>400°C) and reusability for up to seven cycles.

**Ethics.** This work did not require ethical approval from a human subject or animal welfare committee.

**Data accessibility.** The datasets supporting this article have been uploaded as part of the electronic supplementary material [86].

**Declaration of AI use.** We have not used AI-assisted technologies in creating this article.

**Authors' contributions.** B.H.: data curation, formal analysis, investigation, methodology, software, writing—original draft; U.R.: conceptualization, formal analysis, funding acquisition, investigation, methodology, project administration, resources, software, supervision, validation, writing—review and editing; M.J.S.: data curation, formal analysis, investigation, methodology, software, writing—review and editing; G.M.S.A.: data curation, formal analysis, writing—original draft; N.H.: formal analysis, investigation, methodology, resources, writing—review and editing; A.C.: data curation, formal analysis, investigation, writing—original draft; C.N.: formal analysis, investigation, methodology, resources, supervision, writing—review and editing.

All authors gave final approval for publication and agreed to be held accountable for the work performed therein.

**Conflict of interest declaration.** We declare we have no competing interests.

**Funding.** This research work received financial support under Insiatif Putra Siswazah from Universiti Putra Malaysia (Kod Project: 9774800).

**Acknowledgements.** The authors wish to express their sincere gratitude to the Centre of Excellence for Research, Value Innovation, and Entrepreneurship (CERVIE), UCSI University, Malaysia, for their support through the Top 2% Scientists Grant (T2S-2026/013).

# References

1. Bai H, Tian J, Talifu D, Okitsu K, Abulizi A. 2022 Process optimization of esterification for deacidification in waste cooking oil: RSM approach and for biodiesel production assisted with ultrasonic and solvent. *Fuel* **318**, 123697. (doi:10.1016/j.fuel.2022.123697)

2. Abu-Ghazala AH, Abdelhady HH, Mazhar AA, El-Deab MS. 2022 Valorization of hazard waste: efficient utilization of white brick waste powder in the catalytic production of biodiesel from waste cooking oil via RSM optimization process. *Renew. Energy* **200**, 1120–1133. (doi:10.1016/j.renene.2022.10.045)
3. Amenaghawon AN, Obahiagbon K, Isesele V, Usman F. 2022 Optimized biodiesel production from waste cooking oil using a functionalized bio-based heterogeneous catalyst. *Clean. Eng. Technol*. **8**, 100501. (doi:10.1016/j.clet.2022.100501)
4. Garg R, Sabouni R, Ahmadipour M. 2023 From waste to fuel: challenging aspects in sustainable biodiesel production from lignocellulosic biomass feedstocks and role of metal organic framework as innovative heterogeneous catalysts. *Ind. Crop. Prod*. **206**, 117554. (doi:10.1016/j.indcrop.2023.117554)
5. Ruatpuia JVL, Changmai B, Pathak A, Alghamdi LA, Kress T, Halder G, Wheatley AEH, Rokhum SL. 2023 Green biodiesel production from Jatropha curcas oil using a carbon-based solid acid catalyst: a process optimization study. *Renew. Energy* **206**, 597–608. (doi:10.1016/j.renene.2023.02.041)
6. Hosseinzadeh-Bandbafha H, Li C, Chen X, Peng W, Aghbashlo M, Lam SS, Tabatabaei M. 2022 Managing the hazardous waste cooking oil by conversion into bioenergy through the application of waste-derived green catalysts: a review. *J. Hazard. Mater*. **424**, 127636. (doi:10.1016/j.jhazmat.2021.127636)
7. Wang F, Xu H, Yu S, Zhu H, Du Y, Zhang Z, You C, Jiang X, Jiang J. 2022 Fe-promoted Ni catalyst with extremely high loading and oxygen vacancy for lipid deoxygenation into green diesel. *Renew. Energy* **197**, 40–49. (doi:10.1016/j.renene.2022.07.079)
8. Chen J, Wang D, Luo F, Yang X, Li X, Li S, Ye Y, Wang D, Zheng Z. 2022 Selective production of alkanes and fatty alcohol via hydrodeoxygenation of palmitic acid over red mud-supported nickel catalysts. *Fuel* **314**, 122780. (doi:10.1016/j.fuel.2021.122780)
9. Kassa Dada T, Vuppaladadiyam A, Xiaofei Duan A, Kumar R, Antunes E. 2022 Probing the effect of Cu-Sr0 loading on catalyst supports (ZSM-5, Y-zeolite, activated carbon, $Al_2O_3$, and $ZrO_2$) for aromatics production during catalytic co-pyrolysis of biomass and waste cooking oil. *Bioresour. Technol*. **360**, 127515. (doi:10.1016/j.biortech.2022.127515)
10. Zdainal Abidin SN, Lee HV, Juan JC, Rahman NA, Taufiq-Yap YH. 2019 Production of green biofuel by using a goat manure supported Ni–Al hydrotalcite catalysed deoxygenation process. *RSC Adv*. **9**, 1642–1652. (doi:10.1039/c8ra07818a)
11. Ding S, Parlett CMA, Fan X. 2022 Recent developments in multifunctional catalysts for fatty acid hydrodeoxygenation as a route towards biofuels. *Mol. Catal*. **523**, 111492. (doi:10.1016/j.mcat.2021.111492)
12. Liu Y, Wu K, Guo X lin, Wang WY, Yang YQ. 2018 A comparison of $MoS_2$ catalysts hydrothermally synthesized from different sulfur precursors in their morphology and hydrodeoxygenation activity. *J. Fuel Chem. Technol*. **46**, 535–542. (doi:10.1016/s1872-5813(18)30023-9)
13. Wang H, Li G, Rogers K, Lin H, Zheng Y, Ng S. 2017 Hydrotreating of waste cooking oil over supported CoMoS catalyst: catalyst deactivation mechanism study. *Mol. Catal*. **443**, 228–240. (doi:10.1016/j.mcat.2017.10.016)
14. Zhang H, Lin H, Wang W, Zheng Y, Hu P. 2014 Hydroprocessing of waste cooking oil over a dispersed nano catalyst: kinetics study and temperature effect. *Appl. Catal. B* **150–151**, 238–248. (doi:10.1016/j.apcatb.2013.12.006)
15. He Z, Wang X. 2012 Hydrodeoxygenation of model compounds and catalytic systems for pyrolysis bio-oils upgrading. *Catal. Sustain. Energy* **1**, 28–52. (doi:10.2478/cse-2012-0004)
16. Mangesh VL *et al*. 2024 Sustainable biofuel synthesis from non-edible oils: a mesoporous ZSM-5/Ni/Pt catalyst approach. *RSC Adv*. **14**, 7728–7739. (doi:10.1039/d4ra00346b)
17. Brillouet S, Baltag E, Brunet S, Richard F. 2014 Deoxygenation of decanoic acid and its main intermediates over unpromoted and promoted sulfided catalysts. *Appl. Catal. B* **148–149**, 201–211. (doi:10.1016/j.apcatb.2013.10.059)
18. Žula M, Grilc M, Likozar B. 2022 Hydrocracking, hydrogenation and hydro-deoxygenation of fatty acids, esters and glycerides: mechanisms, kinetics and transport phenomena. *Chem. Eng. J*. **444**, 136564. (doi:10.1016/j.cej.2022.136564)
19. Zamani AS, Saidi M, Najafabadi AT. 2023 Selective production of diesel-like alkanes via Neem seed oil hydrodeoxygenation over $Ni/MgSiO_3$ catalyst. *Renew. Energy* **209**, 462–470. (doi:10.1016/j.renene.2023.04.005)
20. Shi F *et al*. 2023 Green diesel-like hydrocarbon production by $H_2$-free catalytic deoxygenation of oleic acid via $Ni/MgO\text{-}Al_2O_3$ catalysts: effect of the metal loading amount. *J. Environ. Chem. Eng*. **11**, 110520. (doi:10.1016/j.jece.2023.110520)
21. de Barros Dias Moreira J, Bastos de Rezende D, Márcia Duarte Pasa V. 2020 Deoxygenation of Macauba acid oil over Co-based catalyst supported on activated biochar from Macauba endocarp: a potential and sustainable route for green diesel and biokerosene production. *Fuel* **269**, 117253. (doi:10.1016/j.fuel.2020.117253)
22. Papageridis K *et al*. 2021 Continuous selective deoxygenation of palm oil for renewable diesel production over Ni catalysts supported on $Al_2O_3$ and $La_2O_2\text{-}Al_2O_2$. *RSC Adv.* **11**, 8569–8584. (doi:10.1039/d0ra08541c)
23. Quintero-Ramos D, Checa M, Jordá JL, Sabater MJ. 2023 Study on the hydrogenation of ethyl stearate to the fatty alcohol 1-octadecanol over Ru on tungstated zirconia. *Catalysts* **13**, 1362. (doi:10.3390/catal13101362)
24. Zulkepli S, Lee HV, Rahman NA, Chuan LT, Show PL, Chen WH, Juan JC. 2022 Highly active iron-promoted hexagonal mesoporous silica (HMS) for deoxygenation of triglycerides to green hydrocarbon-like biofuel. *Fuel* **308**, 121860. (doi:10.1016/j.fuel.2021.121860)
25. Hou Y, Hu W, Zhou X, Gui Z, Hu Y. 2017 Vertically aligned nickel 2-methylimidazole metal–organic framework fabricated from graphene oxides for enhancing fire safety of polystyrene. *Ind. Eng. Chem. Res*. **56**, 8778–8786. (doi:10.1021/acs.iecr.7b01906)
26. Tomar S, Singh VK. 2021 Review on synthesis and application of MIL-53. *Mater. Today* **43**, 3291–3296. (doi:10.1016/j.matpr.2021.02.179)
27. Wang X. 2018 Constructing $NiCo/Fe_3O_4$ heteroparticles within MOF-74 for efficient oxygen evolution reactions. *J. Am. Chem. Soc.* **140**, 15336–15341. (doi:10.1021/jacs.8b08744)

28. Pangestu T, Kurniawan Y, Soetaredjo FE, Santoso SP, Irawaty W, Yuliana M, Hartono SB, Ismadji S. 2019 The synthesis of biodiesel using copper based metal-organic framework as a catalyst. *J. Environ. Chem. Eng*. **7**, 103277. (doi:10.1016/j.jece.2019.103277)
29. Shi H, Shu S, Wang Z, Zhang X, Gu X, Chen J. 2024 Efficient and robust ultrathin porous carbon encapsulated Ni–Sn intermetallic compounds derived from metal–organic frameworks for in-situ aqueous phase deoxygenation of fatty acid methyl esters. *J. Energy Inst.* **114**, 101587. (doi:10.1016/j.joei.2024.101587)
30. Zhang Y, Zhang X, Guo F, Tan KB, Wang Y, Sun K, Rao X, Zhang X, Zhan G. 2023 Fabrication of NiZn bimetallic oxides catalysts supported on carbon black waste for catalytic pyrolysis of fatty acid. *Appl. Catal*. **668**, 119478. (doi:10.1016/j.apcata.2023.119478)
31. Du Y, Wang F, Xia X, Zhu H, Zhang Z, You C, Jiang X, Jiang J, Li C. 2022 MOF-derived Co nanoparticle on nitrogen-rich carbon for fatty acid hydrotreatment into green diesel. *Renew. Energy* **198**, 246–253. (doi:10.1016/j.renene.2022.08.019)
32. Safa-Gamal M, Asikin-Mijan N, Arumugam M, Khalit WNAW, Nur Azreena I, Hafez FS, Taufiq-Yap YH. 2021 Catalytic deoxygenation by $H_2$-free single-step conversion of free fatty acid feedstock over a Co-Ag carbon-based catalyst for green diesel production. *J. Anal. Appl. Pyrolysis* **160**, 105334. (doi:10.1016/j.jaap.2021.105334)
33. Li G, Zhang Y, Hu X, Tan W, Li J, Su D, Wang H, Yang M. 2023 A study on the performance of a novel adsorbent UiO-66 modified by a nickel on removing tetracycline in wastewater. *Chemosphere* **338**, 139399. (doi:10.1016/j.chemosphere.2023.139399)
34. Tamjidi S, Kamyab Moghadas B, Esmaeili H. 2022 Ultrasound-assisted biodiesel generation from waste edible oil using $CoFe_2O_4$@GO as a superior and reclaimable nanocatalyst: optimization of two-step transesterification by RSM. *Fuel* **327**, 125170. (doi:10.1016/j.fuel.2022.125170)
35. Dou Y, Zhang H, Zhou A, Yang F, Shu L, She Y, Li JR. 2018 Highly efficient catalytic esterification in an $-SO_3H$-functionalized Cr(III)-MOF. *Ind. Eng. Chem. Res.* **57**, 8388–8395. (doi:10.1021/acs.iecr.8b01239)
36. Alshorifi FT, Tobbala DE, El-Bahy SM, Nassan MA, Salama RS. 2022 The role of phosphotungstic acid in enhancing the catalytic performance of UiO-66 (Zr) and its applications as an efficient solid acid catalyst for coumarins and dihydropyrimidinones synthesis. *Catal. Commun*. **169**, 106479. (doi:10.1016/j.catcom.2022.106479)
37. Rezaei N, Taghizadeh M. 2024 Pd–Pt promoted HPMo/UiO-66 acid catalyst for n-hexane hydroisomerization for higher quality and cleaner fuel production: catalytic activity and kinetic modeling. *Int. J. Hydrog. Energy* **49**, 892–906. (doi:10.1016/j.ijhydene.2023.07.334)
38. Hao Y, Wang Y, Ren Z, Shen H, Sheng J, Zhang K, Wang J, Wang X. 2023 Preparation of ILe@Cu@MOF catalyst and its application in biodiesel catalysis. *Coatings* **13**, 1437. (doi:10.3390/coatings13081437)
39. Shaik MR, Adil SF, ALOthman ZA, Alduhaish OM. 2022 Fumarate based metal–organic framework: an effective catalyst for the transesterification of used vegetable oil. *Crystals* **12**, 151. (doi:10.3390/cryst12020151)
40. Fiaz M, Athar M, Rani S, Najam-ul-Haq M, Farid MA. 2020 One pot solvothermal synthesis of $Co_3O_4$@UiO-66 and CuO@UiO-66 for improved current density towards hydrogen evolution reaction. *Mater. Chem. Phys*. **239**, 122320. (doi:10.1016/j.matchemphys.2019.122320)
41. Carneiro AC, Meneguin J, dos Santos P, Corazza M, Prete MC, Rinaldi AW, Tarley CR. 2022 On-line micro-packed column solid-phase extraction of cadmium using metal-organic framework (MOF) UiO-66 with posterior determination by TS-FF-AAS. *J. Braz. Chem. Soc*. (doi:10.21577/0103-5053.20220049)
42. Yu D, Duan C, Gu B. 2023 UiO-66-$NH_2$@$MnFe_2O_4$ as a novel and retrievable MOF nanocatalyst for biodiesel synthesis from utilized edible oil in a microwave reactor: RSM design and CI engine studies. *Renew. Energy* **219**, 119338. (doi:10.1016/j.renene.2023.119338)
43. Yoon SY, Choong CE, Nam SN, Park CM, Yoon Y, Choi EH, Jang M. 2024 Preparation of granulated UIO-66/graphene oxide using polyacrylamide/polyvinyl alcohol for selective fluoride removal: mechanism studies via in situ surface-enhanced raman spectroscopy analysis and continuous-flow column operation. *Chem. Eng. J.* **490**, 151217. (doi:10.1016/j.cej.2024.151217)
44. Wu M, Tse JS, Pan Y. 2016 Anomalous bond length behavior and a new solid phase of bromine under pressure. *Sci. Rep*. **6**, 25649. (doi:10.1038/srep25649)
45. Chen C, Liu P, Xia H, Jiang J, Yang X, Zhou M. 2021 Catalytic conversion of lignin to liquid fuels with an improved H/Ceff value over bimetallic NiMo-MOF-derived catalysts. *ACS Sustain. Chem. Eng.* **9**, 13937–13952. (doi:10.1021/acssuschemeng.1c05273)
46. Li S *et al*. 2023 Graphene-based magnetic composite foam with hierarchically porous structure for efficient microwave absorption. *Carbon* **207**, 105–115. (doi:10.1016/j.carbon.2023.02.066)
47. Cai X, Pan J, Tu G, Fu Y, Zhang F, Zhu W. 2018 Pd/UiO-66(Hf): a highly efficient heterogeneous catalyst for the hydrogenation of 2,3,5-trimethylbenzoquinone. *Catal. Commun*. **113**, 23–26. (doi:10.1016/j.catcom.2018.05.010)
48. Xu W, Dong M, Di L, Zhang X. 2019 A facile method for preparing UiO-66 encapsulated Ru catalyst and its application in plasma-assisted $CO_2$ methanation. *Nanomaterials* **9**, 1432. (doi:10.3390/nano9101432)
49. Thai LH, Thanh Nhi LT, Hiep NM, Khan DT, Dat TN, Truong Son LV, Sinh LH. 2025 All-in-one high performance electrochromic device from new photocurable methacrylated viologen and polyaniline/UiO-66/NiO/ZnO composite. *Mater. Today Chem*. **43**, 102511. (doi:10.1016/j.mtchem.2025.102511)
50. Ma T, Liu D, Liu Z, Xu J, Dong Y, Chen G, Yun Z. 2022 12-Tungstophosphoric acid-encapsulated metal-organic framework UiO-66: a promising catalyst for the esterification of acetic acid with n-butanol. *J. Taiwan Inst. Chem. Eng*. **133**, 104277. (doi:10.1016/j.jtice.2022.104277)
51. Li H, Chu H, Ma X, Wang G, Liu F, Guo M, Lu W, Zhou S, Yu M. 2021 Efficient heterogeneous acid synthesis and stability enhancement of UiO-66 impregnated with ammonium sulfate for biodiesel production. *Chem. Eng. J*. **408**, 127277. (doi:10.1016/j.cej.2020.127277)
52. Zhu P, Cao H, Yang H, Geng M, Qin S, Tan L, Gao X, Wang C. 2024 One-pot synthesis of Ni(II)-doped UiO-66-$NH_2$ for enhanced photocatalytic $CO_2$ reduction to CO with efficient charge transfer. *Appl. Surf. Sci*. **652**, 159348. (doi:10.1016/j.apsusc.2024.159348)

53. Ramu AG, Kumari MLA, Elshikh MS, Alkhamis HH, Alrefaei AF, Choi D. 2021 A facile and green synthesis of CuO/NiO nanoparticles and their removal activity of toxic nitro compounds in aqueous medium. *Chemosphere* **271**, 129475. (doi:10.1016/j.chemosphere.2020.129475)
54. Hengne A *et al*. 2018 Ni–Sn-supported $ZrO_2$ catalysts modified by indium for selective $CO_2$ hydrogenation to methanol. *ACS Omega* **3**, 3688–3701. (doi:10.1021/acsomega.8b00211)
55. Casamassima M, Darque-Ceretti E, Etcheberry A, Aucouturier M. 1993 Correlation between Lewis donor/acceptor properties determined by XPS and Brönsted acid/base properties determined by rest-potential measurements, for aluminium and silicon oxides. *J. Mater. Sci*. **28**, 3997–4002. (doi:10.1007/bf00351220)
56. Zhang Y, Li Z, Du W, Chen K, Chu K. 2024 Efficient nitrite-to-ammonia electroreduction over Zr-Ni frustrated Lewis acid-base pairs. *Sci. China Chem*. **67**, 1707–1714. (doi:10.1007/s11426-023-1924-7)
57. Jiang J, Yaghi OM. 2015 Brønsted acidity in metal–organic frameworks. *Chem. Rev*. **115**, 6966–6997. (doi:10.1021/acs.chemrev.5b00221)
58. Lee JH, Kim WJ, Park D, Jo Y, Baik JH, Suh YW. 2024 Zirconia-incorporated yttria with a Lewis pair of acid–base surface sites for chemoselective dehydration of alcohols into alpha olefins. *Appl. Catal*. **678**, 119707. (doi:10.1016/j.apcata.2024.119707)
59. Yang CM, Huynh MV, Liang TY, Le TK, Kieu Xuan Huynh T, Lu SY, Tsai DH. 2022 Metal-organic framework-derived Mg-Zn hybrid nanocatalyst for biodiesel production. *Adv. Powder Technol*. **33**, 103365. (doi:10.1016/j.apt.2021.11.017)
60. Tatay S *et al*. 2023 Synthetic control of correlated disorder in UiO-66 frameworks. *Nat. Commun*. **14**, 6962. (doi:10.1038/s41467-023-41936-w)
61. Zeng D, Li Y, Xia T, Cui F, Zhang J. 2022 MOF-derived $Co_3O_4$ nanoparticles catalyzing hydrothermal deoxygenation of fatty acids for alkane production. *ACS Omega* **7**, 33482–33490. (doi:10.1021/acsomega.2c04382)
62. Meemanah T, Chotirattanachote A, Ahmad J, Rashid U, Ngamcharussrivichai C. 2023 Bifunctional acid–base strontium–titanium mixed oxides supported on SBA-15 for selective synthesis of renewable branched bio-jet fuel precursor. *Fuel* **351**, 128895. (doi:10.1016/j.fuel.2023.128895)
63. Wan Khalit WNA, Asikin-Mijan N, Marliza TS, Safa-Gamal M, Shamsuddin MR, Azreena IN, Saiman MI, Taufiq-Yap YH. 2022 One-pot decarboxylation and decarbonylation reaction of waste cooking oil over activated carbon supported nickel-zinc catalyst into diesel-like fuels. *J. Anal. Appl. Pyrolysis* **164**, 105505. (doi:10.1016/j.jaap.2022.105505)
64. Azreena IN *et al*. 2021 A promoter effect on hydrodeoxygenation reactions of oleic acid by zeolite beta catalysts. *J. Anal. Appl. Pyrolysis* **155**, 105044. (doi:10.1016/j.jaap.2021.105044)
65. Yu C, Yu S, Li L, Li S. 2022 Highly stable Mo-based catalysts for selective hydrodeoxygenation to produce diesel-like hydrocarbons. *Fuel* **323**, 124334. (doi:10.1016/j.fuel.2022.124334)
66. Hunsiri W, Chaihad N, Ngamcharussrivichai C, Tungasmita DN, Reubroycharoen P, Hinchiranan N. 2023 Branched-chain biofuels derived from hydroisomerization of palm olein using Ni/modified beta zeolite catalysts for biojet fuel production. *Fuel Process. Technol*. **248**, 107825. (doi:10.1016/j.fuproc.2023.107825)
67. Chueaphetr R, Suwannaruang T, Khunphonoi R, Khemthong P, Wantala K. 2023 Enhancing deoxygenation of waste cooking palm oil over CaO-MgO catalyst modified by $K_2O$ for green bio-fuel. *Fuel* **354**, 129350. (doi:10.1016/j.fuel.2023.129350)
68. Chen S, Leng M, Liao Z, Zeng J, Xie H, Zhou G. 2024 Synergistic effects of surface acidity and alkalinity of Ni/γ-$Al_2O_3$ catalysts in fats and oils hydrodeoxygenation product distribution. *Ind. Crop. Prod*. **211**, 118227. (doi:10.1016/j.indcrop.2024.118227)
69. Witri Wahyu Lestari WWL, Arifti Nur Laily Aqna A, Fauzan Ibnu Prihadiyono FIP, Riandy Putra RP, Maulidan Firdaus MF, Venansia Avelia Rosari VAR, Ubed Sonai Fahrudin Arrozi U, Grandprix TM Kadja G. 2022 Zirconium(IV)-BTC-based MOF modified with nickel as a catalyst for hydrogenation of citronellal. *JSM* **51**, 2937–2954. (doi:10.17576/jsm-2022-5109-16)
70. Safa Gamal M, Asikin-Mijan N, Arumugam M, Rashid U, Taufiq-Yap YH. 2019 Solvent-free catalytic deoxygenation of palm fatty acid distillate over cobalt and manganese supported on activated carbon originating from waste coconut shell. *J. Anal. Appl. Pyrolysis* **144**, 104690. (doi:10.1016/j.jaap.2019.104690)
71. Li X, Luo X, Jin Y, Li J, Zhang H, Zhang A, Xie J. 2018 Heterogeneous sulfur-free hydrodeoxygenation catalysts for selectively upgrading the renewable bio-oils to second generation biofuels. *Renew. Sustain. Energy Rev*. **82**, 3762–3797. (doi:10.1016/j.rser.2017.10.091)
72. Wang J *et al*. 2023 Highly stable Mo-based bimetallic catalysts for selective deoxygenation of oleic acid to fuel-like hydrocarbons. *J. Environ. Chem. Eng*. **11**, 109104. (doi:10.1016/j.jece.2022.109104)
73. Hu W, Wang H, Lin H, Zheng Y, Ng S, Shi M, Zhao Y, Xu R. 2019 Catalytic decomposition of oleic acid to fuels and chemicals: roles of catalyst acidity and basicity on product distribution and reaction pathways. *Catalysts* **9**, 1063. (doi:10.3390/catal9121063)
74. Santillan-Jimenez E, Morgan T, Lacny J, Mohapatra S, Crocker M. 2013 Catalytic deoxygenation of triglycerides and fatty acids to hydrocarbons over carbon-supported nickel. *Fuel* **103**, 1010–1017. (doi:10.1016/j.fuel.2012.08.035)
75. Aziz I, Sugita P, Darmawan N, Dwiatmoko AA, Rustyawan W. 2024 Hydrodeoxygenation of palm fatty acid distillate (PFAD) over natural zeolite-supported nickel phosphide catalyst: insight into Ni/P effect. *Case Stud. Chem. Environ. Eng.* **9**, 100571. (doi:10.1016/j.cscee.2023.100571)
76. Asikin-Mijan N, Lee HV, Taufiq-Yap YH, Abdulkrem-Alsultan G, Mastuli MS, Ong HC. 2017 Optimization study of $SiO_2$-$Al_2O_3$ supported bifunctional acid–base NiO-CaO for renewable fuel production using response surface methodology. *Energy Convers. Manag*. **141**, 325–338. (doi:10.1016/j.enconman.2016.09.041)
77. Sabino J, Liborio DO, Arias S, Gonzalez JF, Barbosa CMBM, Carvalho FR, Frety R, Barros ICL, Pacheco JGA. 2023 Hydrogen-free deoxygenation of oleic acid and industrial vegetable oil waste on CuNiAl catalysts for biofuel production. *Energies* **16**, 6131. (doi:10.3390/en16176131)
78. Fu L, Li Y, Cui H, Ba W, Liu Y. 2021 Highly stable and selective catalytic deoxygenation of renewable bio-lipids over Ni/$CeO_2$-$Al_2O_3$ for n-alkanes. *Appl. Catal*. **623**, 118258. (doi:10.1016/j.apcata.2021.118258)
79. Chen J, Shi H, Li L, Li K. 2014 Deoxygenation of methyl laurate as a model compound to hydrocarbons on transition metal phosphide catalysts. *Appl. Catal. B* **144**, 870–884. (doi:10.1016/j.apcatb.2013.08.026)

80. Chumuang N, Punsuvon V. 2017 Response surface methodology for biodiesel production using calcium methoxide catalyst assisted with tetrahydrofuran as cosolvent. *J. Chem.* **2017**, 4190818. (doi:10.1155/2017/4190818)
81. Zhang Q, Luo Q, Yang X, Wu Y, Yang B, Wang J, Zhang Y. 2021 Metal–organic framework-derived nanoporous titanium dioxide–heteropoly acid composites and its application in esterification. *Green Process. Synth.* **10**, 284–294. (doi:10.1515/gps-2021-0029)
82. Gamal MS, Asikin-Mijan N, Khalit WNAW, Arumugam M, Izham SM, Taufiq-Yap YH. 2020 Effective catalytic deoxygenation of palm fatty acid distillate for green diesel production under hydrogen-free atmosphere over bimetallic catalyst CoMo supported on activated carbon. *Fuel Process. Technol.* **208**, 106519. (doi:10.1016/j.fuproc.2020.106519)
83. Hazmi B, Rashid U, Kawi S, Mokhtar WNAW, Yaw TCS, Moser BR, Alsalme A. 2022 Palm fatty acid distillate esterification using synthesized heterogeneous sulfonated carbon catalyst from plastic waste: characterization, catalytic efficacy and stability, and fuel properties. *Process Saf. Environ. Prot.* **162**, 1139–1151. (doi:10.1016/j.psep.2022.05.001)
84. Abdullah RF, Rashid U, Hazmi B, Ibrahim ML, Tsubota T, Alharthi FA. 2022 Potential heterogeneous nano-catalyst via integrating hydrothermal carbonization for biodiesel production using waste cooking oil. *Chemosphere* **286**, 131913. (doi:10.1016/j.chemosphere.2021.131913)
85. Aliana-Nasharuddin N, Asikin-Mijan N, Abdulkareem-Alsultan G, Saiman MI, Alharthi FA, Alghamdi AA, Taufiq-Yap YH. 2020 Production of green diesel from catalytic deoxygenation of chicken fat oil over a series binary metal oxide-supported MWCNTs. *RSC Adv.* **10**, 626–642. (doi:10.1039/c9ra08409f)
86. Hazmi B *et al*. 2025 Supplementary material from: Carbonized UiO-66 with Ni nanoparticles for PFAD deoxygenation to green diesel hydrocarbons: Characterization, optimization and deactivation analysis. Figshare. (doi:10.6084/m9.figshare.c.8156466)